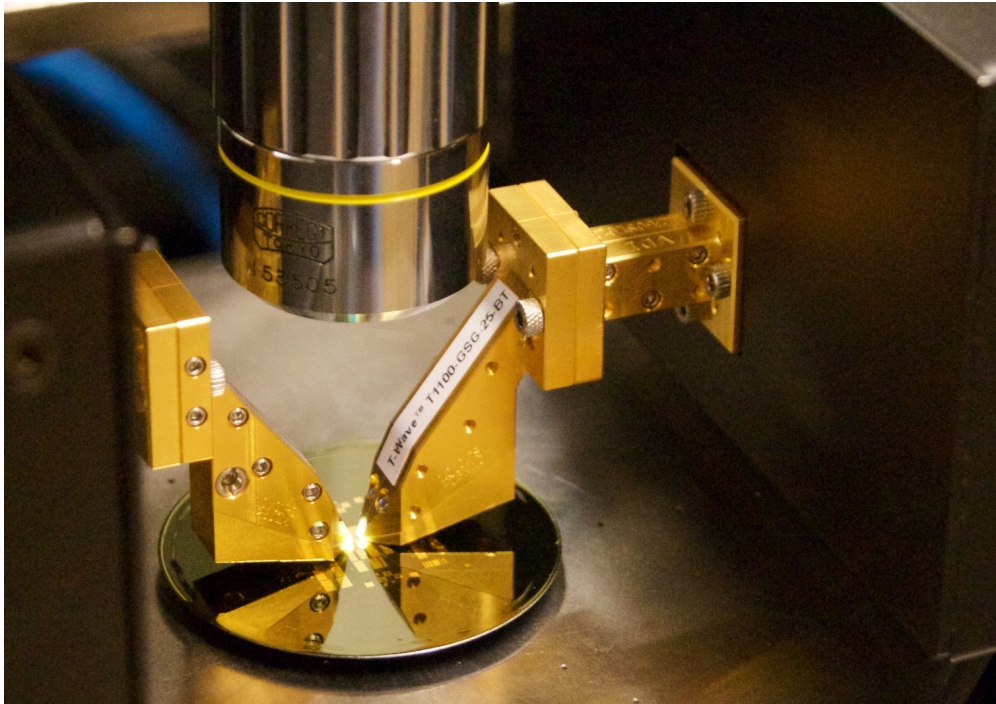




**CHALMERS**  
UNIVERSITY OF TECHNOLOGY

---



# **Design, fabrication and measurements of planar Goubau lines from 0.75 THz to 1.1 THz**

Thesis for the Master of Science in Wireless, Photonics and Space Engineering

**JUAN CABELLO SANCHEZ**



# Design, fabrication and measurements of planar Goubau lines from 0.75 THz to 1.1 THz

JUAN CABELLO SÁNCHEZ



**CHALMERS**  
UNIVERSITY OF TECHNOLOGY

Terahertz and Millimetre Wave Laboratory  
Department of Microtechnology and Nanoscience  
CHALMERS UNIVERSITY OF TECHNOLOGY  
Gothenburg, Sweden 2017

Design, fabrication and measurements of planar Goubau lines from 0.75 THz to 1.1 THz

JUAN CABELLO SÁNCHEZ

© JUAN CABELLO SANCHEZ, 2017.

Supervisor and Examiner: Helena Rodilla, MC2

Terahertz and Millimetre Wave Laboratory  
Department of Microtechnology and Nanoscience  
Chalmers University of Technology  
SE-412 96 Gothenburg  
Telephone +46 31 772 1000

Cover: RF-probe measurements set-up used for calculating the scattering parameters of the fabricated structures.

Typeset in L<sup>A</sup>T<sub>E</sub>X  
Gothenburg, Sweden 2017

Design, fabrication and measurement of planar Goubau lines from 0.75 THz to 1.1 THz

JUAN CABELLO SÁNCHEZ

Department of Microtechnology and Nanoscience

Chalmers University of Technology

## Abstract

Terahertz (THz) waves have proven to possess a unique interaction with biomolecules, and therefore it's interesting to study its influence using biosensors. Recent advances in heterodyne technology allow measuring on-wafer scattering parameters with Vector Network Analysers (VNA) up to 1.1 THz, which could be used for THz molecular spectroscopy. Compared to THz-Time Domain Spectroscopy (THz-TDS), this technique is expected to have greater sensitivity and dynamic range which would open new possibilities for near-field biomolecular spectroscopy. One possible set-up for near-field biosensing is using an on-wafer biosensor, which integrates microfluidic channels for the samples and electrical devices for the sensing. The Planar Goubau Line (PGL), a single conductor waveguide, has suitable properties for near-field on-wafer sensing since its geometry allows a correct sample deposition and a substantial part of the field travels on top of the substrate, where the samples will be located, thus increasing sensitivity.

In this thesis, Planar Goubau Lines (PGL) have been designed, fabricated and measured for frequencies from 0.75 THz to 1.1 THz to be integrated as the electrical structure in a future on-wafer THz biosensor. Additionally, a design method for the layout of the Coplanar Waveguide (CPW) to PGL transition, needed for Ground-Signal-Ground (GSG) probe excitation, was developed to minimise reflections. Electromagnetic simulations were used for the design and analysis of the structures, and different software and port excitations were compared to achieve an accurate simulation environment. The importance of the choice of the substrate's properties is investigated to increase the field on top of the substrate, reduce losses and limit the excitation of substrate modes. The fabrication process is described together with the VNA on-wafer S-parameter measurement set-up.

To obtain conclusions for future optimisation of the structures, the fabricated structures were characterised, and different PGL widths and several CPW-PGL transitions were compared between 0.75 THz and 1.1 THz. In this frequency range, losses showed to be on average 5 dB/mm and 13.3 dB/mm for CPW and PGL, respectively. Despite the high losses per unit length happening at THz frequencies, the small size of the microfluidic channels allows its application in biosensing. The thesis shows that the transmission could be improved by eliminating the carrier wafer, limiting the use of the PGL to the sensing areas and shortening the CPW-PGL transitions. These guidelines would increase the signal-to-noise ratio for the sensor, increasing its potential to analyse THz-biomolecule interaction.

Keywords: Terahertz, WR1, Planar Goubau lines, mode launchers, on-wafer probe measurements, BCB, biosensors, lab-on-a-chip, impedance transformers.



## Acknowledgements

I would like to express my gratitude towards all people who have helped or guided me to produce this master thesis. First, to my supervisor Dr Helena Rodilla for the support, guidance and discussions which allowed to contrast ideas and move forward in the right direction. To Professor Jan Stake, who gave me the opportunity to work at the Terahertz and Millimetre-wave Laboratory where I have learned to put knowledge into practice and gain experience. To Vladimir Drakinskiy and Anna Kim for helping me during the fabrication process in the cleanroom, teaching me during the process and providing me with good advice. And finally to my colleagues in the department and master program, which by discussing ideas and asking for advice have aided me in fields where I am not as experienced.

Juan, Gothenburg, June 2017



## Acronyms

BCB	–	Benzocyclobutene
CPW	–	Coplanar Waveguide
CST	–	Computer Simulation Technology (commercial EM simulation software)
dB	–	Decibel
dBm	–	Decibels with respect to a milliwatt
DUT	–	Device Under Test
e-beam	–	electron-beam lithography
EM	–	Electromagnetic
FEM	–	Finite Element Method
FIT	–	Finite Integration Technique
GSG	–	Ground-Signal-Ground
HFSS	–	High Frequency Structural Simulator (commercial EM simulation software)
IF	–	Intermediate Frequency
LO	–	Local Oscillator
PGL	–	Planar Goubau Line
RF	–	Radio Frequency
TDS	–	Time-Domain Spectroscopy
TE	–	Transverse Electric
TEM	–	Transverse Electromagnetic
THz	–	Terahertz
TM	–	Transverse Magnetic
TRL	–	Through-Reflect-Line
UV	–	Ultraviolet
VNA	–	Vector Network Analyser



# Contents

<b>List of Figures</b>	<b>xiii</b>
<b>List of Tables</b>	<b>xvii</b>
<b>1 Introduction</b>	<b>1</b>
<b>2 Theory</b>	<b>3</b>
2.1 Scattering parameters . . . . .	3
2.2 Theory of small-reflections . . . . .	4
2.3 Coplanar waveguide (CPW) . . . . .	5
2.4 Goubau line . . . . .	6
2.5 Planar Goubau line (PGL) . . . . .	7
2.6 Substrate modes . . . . .	8
<b>3 Method</b>	<b>9</b>
3.1 Simulation . . . . .	9
3.1.1 FEM vs. FIT . . . . .	9
3.1.2 Simulation of CPW port . . . . .	10
3.1.3 Simulation of PGL port . . . . .	11
3.2 Design of PGL . . . . .	14
3.2.1 Choice of the substrate . . . . .	15
3.2.2 Width of the PGL . . . . .	16
3.3 Design of CPW to PGL transition . . . . .	17
3.3.1 Design of probing CPW . . . . .	18
3.3.2 Design of tapered CPW . . . . .	19
3.3.3 Design of PGL launcher . . . . .	22
3.4 Fabrication process . . . . .	23
3.5 Measurement's set-up . . . . .	25
3.5.1 Calibration . . . . .	26
<b>4 Results</b>	<b>29</b>
4.1 Repeatability of the measurements . . . . .	29
4.2 Simulations vs. measurements . . . . .	30
4.3 Characterisation of the PGL . . . . .	31
4.3.1 3mm long PGL . . . . .	31
4.3.2 Length of the CPW and PGL . . . . .	32
4.3.3 Width of the PGL . . . . .	33

4.3.4	Length of the tapered CPW . . . . .	34
4.3.5	Length of the PGL launcher . . . . .	36
<b>5</b>	<b>Conclusion</b>	<b>37</b>
	<b>Bibliography</b>	<b>39</b>

# List of Figures

2.1	Multi-section transmission line followed by resistor. $Z_n$ is the characteristic impedance of the line $n$ and $\Gamma_n$ is the partial reflection coefficient between lines $n$ and $n + 1$ . . . . .	4
2.2	(a) CPW cross section and (b) CPW line. . . . .	5
2.3	CPW modes: (a) desired even mode and (b) radiative odd mode. . . . .	6
2.4	PGL: a metal strip deposited on top of a substrate. (a) PGL design parameters. (b) PGL's cross section together with the Goubau mode's radial electric field. . . . .	7
3.1	Comparison of a wave port of the same dimensions ( $80 \mu\text{m} \times 126 \mu\text{m}$ ) on (a) HFSS and (b) CST. It can be seen that CST excites an even CPW mode, while HFSS excites a hybrid mode. . . . .	10
3.2	Discrete port used in CST, where a conducting plane was use to connect the two CPW grounds . . . . .	11
3.3	(a) Impedance vs. ratio of outer/inner conductor radii for an ordinary coaxial cable and a dielectric-coated inner conductor coaxial cable, as depicted in Goubau's study.(b) The impedance values vs. port size as calculated with the developed PGL port in CST. . . . .	12
3.4	CST simulation results of (a) $S_{11}$ and (b) $S_{21}$ of a $1 \mu\text{m}$ wide and $3 \text{ mm}$ long PGL deposited on a $30 \mu\text{m}$ thick BCB substrate for different port sizes. Results show to converge when the size of the port is increased. . . . .	13
3.5	PGL port validity simulation, where a CPW-PGL-CPW structure (a) and half of the same structure using the PGL port (b) were simulated and compared in Fig. 3.6. The PGL port is square-shaped with side length of $L$ . . . . .	13
3.6	CST simulation results of (a) $S_{11}$ and (b) $S_{21}$ of the structures represented in Fig. 3.5. . . . .	14
3.7	Simulated PGL characteristic impedance vs. PGL width, using the PGL port in CST. . . . .	14
3.8	CST simulation results of (a) $S_{11}$ and (b) $S_{21}$ for a $3 \text{ mm}$ long PGL on a $30 \mu\text{m}$ thick BCB substrate with (in red) and without (in blue) a supporting $300 \mu\text{m}$ high-resistivity silicon substrate below the BCB. . . . .	16
3.9	CST simulation results of (a) $S_{11}$ and (b) $S_{21}$ of $3 \text{ mm}$ long a PGL of different widths: $1 \mu\text{m}$ (blue), $3 \mu\text{m}$ (red) and $9 \mu\text{m}$ (green). . . . .	17

3.10	CPW to PGL transition split in its three section. (a) Layout of transition. (b) Transmission line model of the CPW-PGL transition, using impedance transformers. . . . .	18
3.11	Designed CPW tapered line. The CPW strip width varies as a cosine function, while the slot width is adjusted to make a smooth impedance transition to minimize reflections. . . . .	19
3.12	Impedance transformer between two arbitrary impedances, $Z_0$ and $Z_{N+1}$ . To model a tapered CPW impedance transformer a high value of $N$ and small value of $\theta$ are taken. . . . .	20
3.13	Reflection vs. total electrical length of a gradual impedance transformer between $Z_0 = 50 \Omega$ and $Z_{N+1} = 120 \Omega$ , modelled as a 1000-section transmission line. Below $-40$ dB reflections can't usually be measured and thus are not plotted. . . . .	21
3.14	Tapered PGL launcher layout, where the central strip has a width of $S_{PGL} = 1 \mu\text{m}$ . $D$ is the final separation of the CPW grounds and $L$ is the length of the launcher, respectively. An additional section was used to end the launcher with soft corners. . . . .	23
3.15	(a) Fabrication steps for e-beam lithography and (b) detail from the fabricated structure, showing 3 mm PGL structures. . . . .	24
3.16	(a) Sketch of on-probe S-parameter measurements used. (b) Probes measuring the structures on the 2-inch BCB/Silicon wafer. (c) View of a tapered CPW being measured with the probes, as seen under the microscope. . . . .	26
4.1	Five (a) $S_{11}$ and (b) $S_{21}$ measurements of the 2.7 mm long PGL structures using the measuring parameters in table 4.1. (Detail) Measurements from the BCB calibration substrate (# 3 to #5) are very repeatable, while the quartz ones (# 1 and #2) deviate more. . . . .	30
4.2	$S_{21}$ results comparison of HFSS (green), CST (red) and VNA measurements (blue) of a 3 mm long CPW (a) and a 3 mm long PGL (b). . . . .	31
4.3	(a) Layout of the 3 mm long PGL. (b) $S_{11}$ (blue) & $S_{22}$ (red) and (c) $S_{12}$ (blue) & $S_{21}$ (red) measurement results. . . . .	32
4.4	(a) Layout of the measured structures in Fig. 4.4 (b). (b) $S_{21}$ measurements of reference (blue), plus 500 $\mu\text{m}$ extra PGL (red) and plus 500 $\mu\text{m}$ extra CPW (green). (c) $S_{21}$ measurements of the reference 3 mm long PGL (red) and a 2.7 mm long PGL (blue), having both the same CPW-PGL transition. . . . .	33
4.5	(a) Layout of the 1 $\mu\text{m}$ and 9 $\mu\text{m}$ wide PGL structures. (b) $S_{21}$ measurements of 1 $\mu\text{m}$ (blue), 3 $\mu\text{m}$ (red) and 9 $\mu\text{m}$ (green) wide PGLs. (c) Simulated $S_{21}$ results of 1 $\mu\text{m}$ (blue), 3 $\mu\text{m}$ (red) and 9 $\mu\text{m}$ (green) wide PGLs using an absorbing condition on the bottom side of the silicon substrate. . . . .	34
4.6	(a) Layout of the measured structures. (b) $S_{11}$ and (c) $S_{21}$ measurements comparison of 250 $\mu\text{m}$ (blue) and 500 $\mu\text{m}$ (red) long tapered CPWs. . . . .	35

4.7 (a) Layout of the measured structures. (b) $S_{11}$ and (c) $S_{21}$ measurements comparison of 250 $\mu\text{m}$ (blue) and 500 $\mu\text{m}$ (red) long PGL launchers. . . . .	36
--------------------------------------------------------------------------------------------------------------------------------------------------------------------------------------	----



# List of Tables

4.1	Parameters used for the measurements. In order, the measurement number in Fig. 4.1, the calibration substrate used for the measurement, the calibration number and the IF bandwidth used. . . . .	29
-----	---------------------------------------------------------------------------------------------------------------------------------------------------------------------------------------------------	----



# 1

## Introduction

Terahertz (THz) waves, spanning between 0.3 THz and 10 THz in the electromagnetic spectrum, lie between the microwave and infrared bands, which already have the mature technologies of electronics and photonics, respectively. When trying to directly produce THz power by scaling these approaches, electronics become limited by carrier mobility and transit time; whereas optical solid-state lasers require cryogenic operation to allow stimulated emission of low energy of THz photons [1]. Up to date, one of the practical ways of producing or detecting energy at THz frequencies is to use non-linear devices to either up-convert microwave signals [2] or down-convert photonic signals [3]. These limitations in sources and detectors are the main reason that has kept this part of the spectrum unexplored compared to its electronics and photonics counterparts, but recent advances in technology are continuously improving the possibilities of THz wave research and its applications.

Traditionally, THz technologies have been used in high-resolution spectroscopy, as many light-weight molecules have spectral lines lying in the THz spectrum [4]. Moreover, approximately half of the luminosity and 98% of all photons emitted since the big bang lie at THz frequencies [5]. The vast information that THz could provide about the universe interested the astronomy community and made their discipline an important driver for THz technology. As new instrumentation was developed, the application of THz waves expanded to many other fields, including high-speed communications [6], security imaging [7] and biology and medicine [8].

Regarding the biological field, THz waves have proven to have a unique interaction with biomolecules. The reason for this is the existence of low-frequency motions of biomolecules at THz frequencies which are believed to play a key role in their biological function [9]. Measuring these vibrational modes could give valuable information about the conformational dynamics of the biomolecules and could be used for their study and identification [10, 11]. THz waves have already been successfully used for analysing protein structure dynamics [9], bio-affinity between biomolecules [12] and characterising genetic material [13], showing high sensitivity while being label-free. Label-free techniques have the advantage of not needing labelling preparatory steps and eliminate the influence of the labels in the measured samples [14].

Traditionally, THz Time Domain Spectroscopy (THz-TDS), based on a photonic approach to THz, has been the dominating technique for performing THz molecular spectroscopy [13]. However, recent advances in heterodyne technology now allow the use of the electronics' approach, using VNA and Ground-Signal-Ground (GSG) RF-probes (up to 1.1 THz [15]), which is expected to have greater sensitivity and dynamic range and thus would open new possibilities for the THz near-field

biosensing. This approach could excite an on-wafer THz biosensor, increasing the maximum frequency of these type of devices which have already been studied at microwaves and millimetre-wave frequencies [16, 17, 18]. In addition to the electrical structures used to guide the THz waves, the on-wafer biosensor would consist of microfluidic channels which would contain the liquid samples providing with control of the sensing environment and limiting the sensing volumes as to reduce the high losses produced by water at THz frequencies [8].

The focus of this thesis was to design, fabricate and measure planar passive structures from 0.75 THz to 1.1 THz for being used in an on-wafer biosensor. The planar structures need to have a substantial part of the field propagating above of the substrate, where the samples will be located, as well as a suitable geometry to allow a correct deposition of the samples. The Planar Goubau Line (PGL), a single conductor waveguide, fulfilled these specifications, and thus was the choice of structure to be used for the sensing area.

One of the main issues of designing planar structures at THz frequencies is the suppression of substrate modes, which cause losses and resonances. To eliminate these modes, the substrate needs to have a thickness in the order of tens of microns and a low permittivity. These ultra-thin substrates can be fabricated by spinning and curing a resin on top of a carrier wafer, but due to their limited thickness, the field of the structures can reach the carrier wafer and therefore its electrical properties also need to be considered to avoid substrate modes. Additionally, having a substrate which allows the propagation of substrate modes causes electromagnetic simulators to have difficulties to excite correctly the structure's mode when the wave port has a recommended size. However, reducing the port's size produces incorrect results, as the conducting boundary at the edge of the port is close enough to interfere the desired mode. For this reason, different electromagnetic simulators and port excitations were studied in order to have an accurate simulation environment for the analysis and design of the structures. Since the RF-probes have a GSG geometry, the structures needed to have Coplanar Waveguide (CPW) for making contact with the probes, and thus a CPW-PGL transition is needed to excite the PGL. This transition is key for an efficient excitation of the Goubau mode in the PGL [19], and therefore a method for designing its layout was developed using transmission line theory to smooth impedance transition and thus minimising reflections. Finally, different structures were fabricated and their S-parameters measured using RF-probes and VNA, to characterise the PGL and CPW losses, PGL's width and the CPW-PGL transition. The key aspects of each part of the thesis are described, following with a discussion of the results and future development lines.

# 2

## Theory

### 2.1 Scattering parameters

When characterising linear electrical circuits much smaller than a wavelength it is common to use the relation between voltages and currents (circuit theory) as these are easily measured. In this type of circuits and for most practical purposes, one can assume that there is an instantaneous propagation of such voltages and currents, which greatly simplify the calculations. However, when the size of the circuit is comparable to the wavelength, not only must one take into account the propagation of the energy through the circuit, but also the concepts of voltage and current might not be easily defined and therefore used. For such conditions, incident and reflected waves from each port are used to describe the energy propagation in the circuit (instead of voltage and current) and their ratios are used to describe the circuit's behaviour. These ratios are called Scattering parameters or S-parameters.

Mathematically, the S-parameters can be defined as follows: let  $a_n$  and  $b_n$  be the phasors representing magnitude and phase of the incident and reflected waves respectively in port  $n$  in an N-port circuit for a given frequency. Then,  $S_{ij}$  is the ratio of the reflected wave in port  $i$ ,  $b_i$ , to the incident wave in port  $j$ ,  $a_j$ , when all other incident waves are set to zero  $a_k = 0 \quad \forall k \neq j$ , or

$$S_{ij} = \left. \frac{b_i}{a_j} \right|_{a_k=0 \quad \forall k \neq j} \quad (2.1)$$

Thus, if a linear circuit is being modelled, one can express the reflected wave in port  $i$  as a sum of all port contributions:

$$b_i = \sum_{n=1}^N S_{in} a_n \quad (2.2)$$

Physically,  $\frac{1}{2}|a_n|^2$  and  $\frac{1}{2}|b_n|^2$  represent the time-average power of the incident and reflected wave respectively. Note how for an N-port circuit which doesn't introduce any additional external power (or passive circuit) it must fulfil:

$$\begin{cases} |S_{ij}| \leq 1 & i, j = 1, 2, \dots, N \\ \sum_{j=1}^N |S_{ij}|^2 \leq 1 & i = 1, 2, \dots, N \end{cases} \quad (2.3)$$

It is important to note that the S-parameters are frequency dependent, and they are usually plotted against this variable, forming a frequency response plot which provides an intuitive representation of the circuit's behaviour. Because of the wide

range of the order of magnitude of the S-parameter module, they are most often expressed using a logarithmic scale, plotting  $20 \log_{10} |S_{ij}|$  instead of the linear scale expression  $|S_{ij}|^2$ .

More theory related with S-parameters can be found in [20, 21]

## 2.2 Theory of small-reflections

The theory of small reflections [21] is an approximation method used to simplify the reflection coefficient analysis. This approximation produces accurate results under conditions of small impedance discontinuities, which causes reflections of small magnitude. The characteristic impedance of a transmission line is the ratio of voltage-to-current magnitudes of a wave travelling in the absence of reflections. A change in the characteristic impedance of the line causes a change in boundary conditions and may excite reflections as a way to satisfy them.

Let us consider  $N$  cascaded transmission lines of equal electrical length,  $\theta$ , terminated on an impedance  $Z_{N+1}$  (see Fig. 2.1). In each of the line interfaces there will be a partial reflection coefficient given by the difference in the impedance of the lines:

$$\Gamma_n = \frac{Z_{n+1} - Z_n}{Z_{n+1} + Z_n} \quad (2.4)$$

where  $\Gamma_n$  is the partial reflection coefficient between the lines  $n$  and  $n + 1$ , and  $Z_n$  is the characteristic impedance of the line  $n$ .

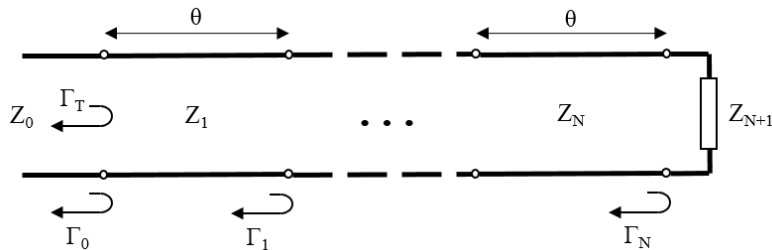


**Figure 2.1:** Multi-section transmission line followed by resistor.  $Z_n$  is the characteristic impedance of the line  $n$  and  $\Gamma_n$  is the partial reflection coefficient between lines  $n$  and  $n + 1$ .

Then, the total reflection coefficient at the start of the line,  $\Gamma_T$ , can be calculated as a sum of all the infinite reflection combinations paths that a wave could have. This solving approach is too complex to be used practically, but if the partial reflections in each interface are low, a powerful approximation, known as "theory of small reflections", can be made. Assuming a small difference in impedance between two consecutive transmission lines, i.e.  $|Z_{n+1} - Z_n| \ll |Z_{n+1} + Z_n|$ , there will be a small reflection at their interface, and therefore  $|\Gamma_n|^2 \ll |\Gamma_n|$ . Then all reflection paths which involve more than one reflection will be much smaller than the single reflections in the circuit, and thus can be ignored in the analysis. Because only an odd

number of reflections can happen, it is guaranteed that  $|\Gamma_n| \gg |\Gamma_n|^3 \gg |\Gamma_n|^5 \gg \dots$ . Then, the total reflection coefficient can be expressed by the sum of all single-reflections paths occurring along the multi-section transmission line:

$$\Gamma_T \simeq \sum_{n=0}^N \Gamma_n e^{-j2\theta n} \quad (2.5)$$

This approximation proves to be very accurate and eliminates the need of making a full analysis.

### 2.3 Coplanar waveguide (CPW)

The Coplanar Waveguide (CPW) [22] is a transmission line which is composed of three parallel metal strips on top of a dielectric substrate, forming a Ground-Signal-Ground configuration. Its design parameters are: strip width ( $s_{CPW}$ ), the slot width ( $w_{CPW}$ ), the substrate height ( $h$ ) and its dielectric constant ( $\epsilon_r$ ) (see Fig. 2.2 (a)). The fact that all conductors are on the same side of the substrate gives the CPW an advantage for several applications, being especially appropriate for active circuits for the ease of connecting transistors, making via-holes unnecessary.

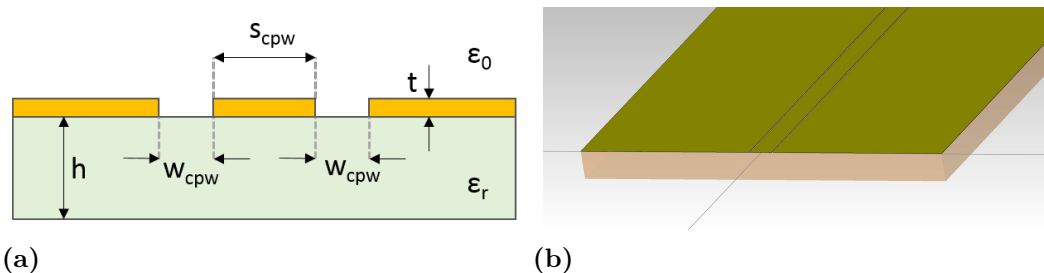


**Figure 2.2:** (a) CPW cross section and (b) CPW line.

The field propagates inside the two gaps between the Ground-Signal conductors, and can have two mode configurations, odd and even (see Fig. 2.3), depending if the electric fields in the gaps have the same or opposite direction. The desired mode is the even mode, which propagates with low losses. If the odd mode is excited it will cause losses in the form of radiation, which increases proportionally to the distance between both ground planes.

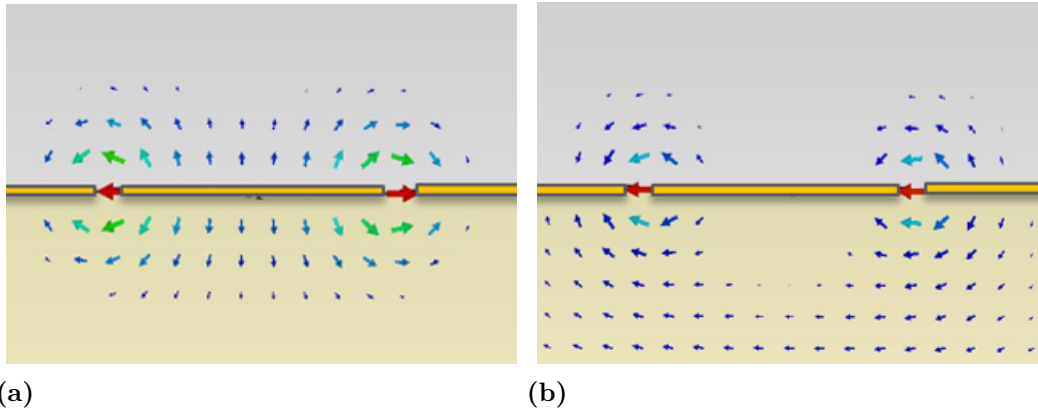


**Figure 2.3:** CPW modes: (a) desired even mode and (b) radiative odd mode.

## 2.4 Goubau line

In 1899, Sommerfeld described the propagation of non-radiative surface mode on a single finite conductor wire, different from the radiating mode occurring in long-wire antennas [23]. The existence of the mode was possible thanks to the roughness and limited conductivity in the wire, and would not exist in a perfectly smooth and perfect conducting wire. To excite this non-radiative mode, one would need to design a mode launcher which would create the same field distribution as the non-radiative mode, and since the field decreases slowly in the radial direction, the launcher would have large dimensions, which could be unpractical. In 1951, Goubau exploited the fact that imperfections in the surface of the wire would convert Sommerfeld's mode into another mode which was determined by surface conditions, which allowed to change the fields extension [24]. By coating the wire with a dielectric layer, one could modify the boundary conditions on the surface and allow to change the extension of the field around the wire, being inversely proportional to the dielectric layer thickness. To achieve a wider bandwidth, a thin and low dielectric permittivity coating is recommended. However, a minimum thickness is needed to obtain the necessary wave propagation delay and confine the field closer to the metallic wire [25]. Dielectric losses will not raise substantially due to higher confinement as most of the power will be propagating outside of the coating.

This line proposed by Goubau is equivalent to a coaxial line with the inner conductor coated in a dielectric and an infinitely large outer conductor. The dielectric coating not only changes the Transverse Electromagnetic Mode (TEM) to Transverse Magnetic (TM) but also eliminates the influence of the outer conductor when being sufficiently large. For designing a mode launcher from a coaxial line, the outer conductor has to be gradually separated forming a conducting cone, and the coaxial would naturally develop into a Goubau line. The size of the radius of the cone should be as large as the field's extension for greater efficiency. The higher the frequency, the more power is concentrated around the wire, thus not requiring as large launchers.

Single-wire transmission lines at THz frequencies [25, 26], have shown the lowest

attenuation coefficient for a transmission line at these frequencies, having an average value smaller than  $0.03 \text{ cm}^{-1}$  [26].

## 2.5 Planar Goubau line (PGL)

The Planar Goubau Line (PGL) [27] is a planar version of the single-conducting-wire dielectric-covered Goubau line (see section 2.4). This waveguide consists of a single conducting strip placed on top of a dielectric substrate (Fig. 2.4 (a)). The main propagation mode is TM, where the electric field is quasi-radial to this conductor (see Fig. 2.4 (b)), being electrically similar to its 3-dimensional counterpart.

While finite conductivity in the wire allows propagation in Sommerfeld's line, the Goubau line's dielectric coating enables the existence of the propagation mode even if the conductivity of the wire is high. In the case of the PGL, the substrate below, acting similarly as the dielectric coating in the Goubau Line, provides the boundary conditions necessary for allowing the propagation mode independently of the conductivity of the metal wire. Transmission lines of two or more conductors, have most of their transmitting power between the conductors, resulting in a highly confined field. Since the PGL has a single conductor, its field naturally spreads over a wider area in its cross-section than most multi-conductor transmission lines.

The PGL needs a planar version of a launcher for exciting its propagation mode [19], and this launcher is a major factor for achieving a high efficiency in the mode-conversion. Because of the geometry of Ground-Signal-Ground (GSG) probes used to excite planar structures at THz frequencies, the transition is done from CPW, where the central strip is made thinner while the ground planes are progressively separated. This process is an equivalent to the Goubau line transition consisting of a coaxial line whose outer conductor is gradually separated: both coaxial and CPW have a field pointing radially from the central conductor.

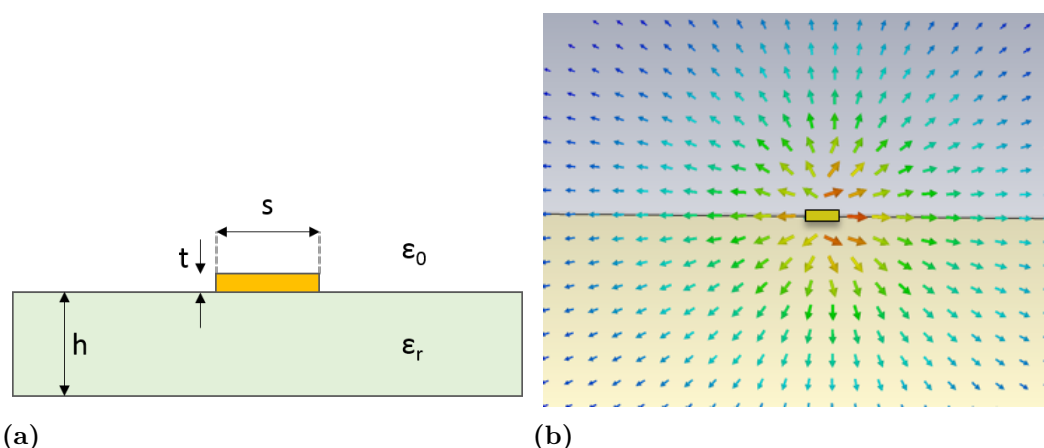


**Figure 2.4:** PGL: a metal strip deposited on top of a substrate. (a) PGL design parameters. (b) PGL's cross section together with the Goubau mode's radial electric field.

As opposed to other transmission lines commonly used at THz frequencies, the

PGL's one-conductor geometry gives it a better sample deposition in the case of being used as a sensor. For example, the CPW could have an inter-conductor gap the size of microns (where the field is confined) and might present practical problems to deposit samples on it.

Experimental measurements below THz frequencies, between 60 GHz and 220 GHz, for a 2.9 mm end to end PGL and have shown a relatively low-loss propagation of  $-6$  dB [19], which proves its viability as waveguide at these frequencies.

Regarding the width of the PGL's strip, the transmission of  $2\ \mu\text{m}$  and  $60\ \mu\text{m}$  wide PGLs were compared in [28] and the  $2\ \mu\text{m}$  wide line had approximately 4 dB higher  $S_{21}$  for the same line length. In the same study, the characteristic impedance of the PGL was estimated to be higher than  $200\ \Omega$ .

## 2.6 Substrate modes

The substrate plays a key role in the electric performance of planar passive structures, and it is defined by the dielectric constant ( $\epsilon_r = \epsilon'_r + j\epsilon''_r$ ) of the material and its thickness. For instance, a higher  $\epsilon'_r$  increases electrical length for a given physical length and confines more the field inside the dielectric. If the frequency is high enough, the substrate can also support modes propagating within it, similarly to a dielectric slab waveguide, which is a dielectric layer having lower permittivity dielectrics on top and bottom. The modes in the dielectric slab waveguide propagate on the higher dielectric permittivity layer confined by the total reflection occurring at the dielectric interface. The modes propagating inside the dielectric are referred as "substrate modes", and are undesirable as they drain power from the desired propagating mode, thus causing losses and complicating the structure's behaviour. The substrate modes are  $TM_n$  and  $TE_n$  and have their cutoff frequency as a function of dielectric thickness and permittivity. As an approximation, the value is calculated from the cut-off frequency of the modes in a dielectric slab waveguide, given by the expressions [29]:

$$TM_n : \quad f_c = \frac{n \cdot c_0}{2 \cdot h \cdot \sqrt{\epsilon'_r - 1}} \quad n = 0, 1, 2, \dots \quad (2.6)$$

$$TE_n : \quad f_c = \frac{(2n - 1) \cdot c_0}{4 \cdot h \cdot \sqrt{\epsilon'_r - 1}} \quad n = 1, 2, \dots \quad (2.7)$$

where  $c_0$  is the speed of light in vacuum,  $h$  is the substrate's thickness and  $\epsilon'_r$  is the real part of the dielectric permittivity. From these equations can be seen that the higher the frequency, the more substrate modes will propagate. As an example, a substrate with  $\epsilon'_r = 5$  and  $h = 150\ \mu\text{m}$  will have approximate dielectric slab mode cut-off frequencies of 0 Hz, 0.5 THz, 1 THz... for the  $TM_n$  modes and 0.25 THz, 0.75 THz, 1.25 THz... for the  $TE_n$  modes. Therefore at THz frequencies is crucial to choose a suitable substrate to avoid the excitation of such modes and avoid losses.

# 3

## Method

This chapter presents the simulation, design, fabrication and measurement's method done for the PGL structures in the frequency band from 0.75 THz to 1.1 THz (WR1.0 band). It starts comparing the different electromagnetic simulators and settings, presenting the characteristics of the proper simulation environment (section 3.1). Later, the PGL design is described (section 3.2) and a layout design method for the CPW-PGL transition based on smooth impedance transformation is explained (section 3.3). Finally, the fabrication method (section 3.4) and measurement set-up (section 3.5) are described.

### 3.1 Simulation

In this thesis, simulations have been used to analyse and gain an understanding of the designed structures. To correctly set-up an electromagnetic simulation environment one must take into account the simulation algorithm, excitation, boundary conditions, material properties, meshing, etc. A comparison between two electromagnetic simulation methods, using commercial software, was done in section 3.1.1. In section 3.1.2 the accuracy of different port excitations were studied for the correct excitation of a CPW line, and in section 3.1.3 the possibility of directly exciting a PGL using a wave port was studied.

#### 3.1.1 FEM vs. FIT

For simulating the PGL, two electromagnetic simulation methods were compared using commercial software: Finite Element Method (FEM) [30] (using Ansys HFSS [31]) and Finite Integration Technique (FIT) [32] (using CST Microwave Studio [33]). The main difference between both software is that they solve Maxwell's equations in different domains: HFSS in the frequency domain and CST in the time domain. Also, in HFSS the meshing is done with tetrahedra while in CST it is done using orthogonal hexahedra, which makes it simpler and faster but might not be as accurate. CST simulates exciting the structure with a pulse and calculates alternatively the electric and the magnetic field over time. It simulates a finite amount of time in which it monitors the outgoing signals in the simulation ports, and by relating the output and the input signals, it can calculate the S-parameters. However, the simulation might not be accurate or take too long simulation time if the structure is resonant or there are several highly reflective elements. On the other hand, HFSS simulates in the frequency domain and therefore solves Maxwell's

equations for specified frequency points. This approach has the benefit of analysing the structures assuming, the usually more relevant, time-harmonic conditions while neglecting transient phase effects that arise at the start of the excitation. Therefore, HFSS is commonly recommended for electrically smaller and resonant structures, while CST is more suitable for larger non-resonant structures.

When applying CST and HFSS to our case, CST gave more consistent results than HFSS while having shorter simulation time, taking about an hour compared to several days for HFSS for a 3 mm long PGL, which made HFSS unpractical. Also, when using a same-size wave port in both simulators, CST excited the even CPW mode correctly while HFSS would only excite undesirable hybrid modes (see Fig. 3.1), which made the excitation non-reliable.

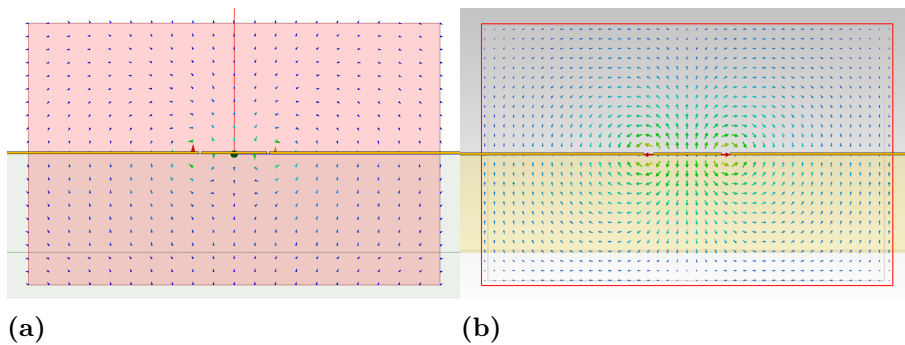


**Figure 3.1:** Comparison of a wave port of the same dimensions ( $80\ \mu\text{m} \times 126\ \mu\text{m}$ ) on (a) HFSS and (b) CST. It can be seen that CST excites an even CPW mode, while HFSS excites a hybrid mode.

#### 3.1.2 Simulation of CPW port

A crucial simulation aspect is to correctly excite the CPW at the start of the CPW-PGL transition. This simulated excitation has to emulate the one being used during the experiments i.e. the even mode. In this thesis two types of excitations were tested for:

- **Wave port:** can be seen as a rectangular waveguide opening the same size as the wave port and with the same materials. It creates the boundary conditions which allow energy to enter and leave the simulation. The size of the port is an important aspect for a correct modelling of the wave port excitation. The port needs to be sufficiently large to cover the cross-section where the field is confined in the transmission line, but not excessively large, which could excite artificial higher order rectangular waveguide modes which propagate in the simulated transmission line and give erroneous results. Since the wave port acts as a rectangular waveguide, its edges behave as conductors and therefore impose a short-circuit, which should be taken into account.
- **Discrete port:** also called lumped port in HFSS, is equivalent to a probe contacting two points and exciting with a current generator which has an internal impedance. This port generates and absorbs power, and uses the generated and reflected signal for calculating the S-parameters of the structure

under simulation. The internal impedance is user-defined and determines the S-parameters measured by this type of port. Because of the CPW's three-conductor geometry, it cannot be excited using a single discrete port. One solution is to connect the two CPW ground planes using a conducting plane behind the CPW line, and to position the discrete port between the CPW line and the connecting plane, as can be seen in Fig. 3.2. This connecting plane between the grounds had an impact on the structure's behaviour, increasing the reflections, and thus made the discrete port analysis method not accurate.

Within CST, the wave port was preferred over the discrete port excitation as it gave more consistent results and required no additional conducting plane connector between the CPW's ground planes.

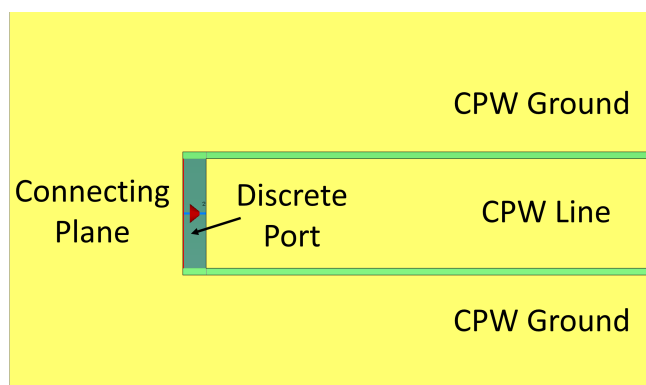


**Figure 3.2:** Discrete port used in CST, where a conducting plane was used to connect the two CPW grounds

### 3.1.3 Simulation of PGL port

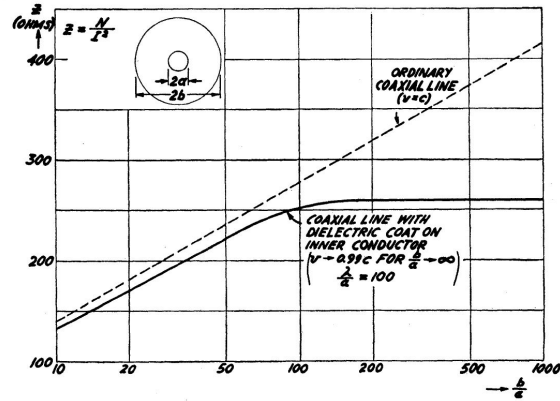
The possibility of exciting the PGL without the need of a CPW-PGL transition would reduce simulation time and provide a better simulation environment for future analysis/synthesis of PGL elements.

A square wave port centred around the PGL was made for exciting the Goubau mode in a line deposited on a 30  $\mu\text{m}$  thick BCB layer. Since the wave port has perfect conducting edges, the excited mode is similar to a square coaxial-line mode. In [24] Goubau explains how a coaxial with an inner conductor coated in dielectric causes the field to have a longitudinal electric component. If the outer conductor radius is increased, there is a point where it no longer changes the field distribution around the inner conductor. As a consequence, the characteristic impedance's value of the dielectric-coated coaxial saturates after a certain outer conductor radius, unlike the uncoated coaxial's impedance which continues to increase logarithmically (Fig. 3.3). Since the PGL has a similar TM mode to the Goubau line, these results suggest that for a sufficiently large wave port both the S-parameter results and the impedance value should converge. To test this supposition:

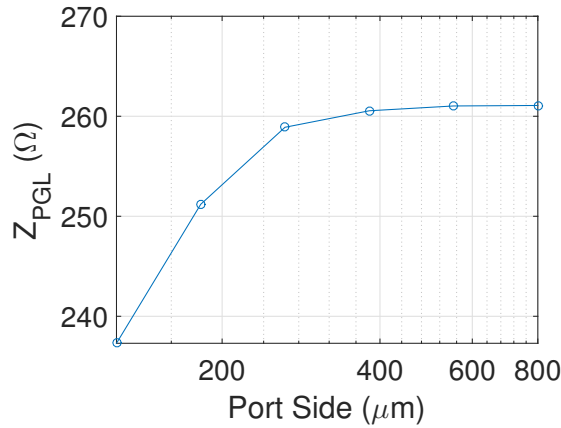
1. The size of the port was increased exponentially, where both S-parameters and port impedance values were monitored until these values would converge to a fixed value. Results can be seen in Fig. 3.4.

### 3. Method

- The port which gave convergent S-parameters and port impedance values was tested. To validate it, the frequency behaviour of two structures were compared: a CPW-PGL-CPW structure (Fig. 3.5 (a)), with two CPW wave ports as inputs, against the same structure cut in half (Fig. 3.5 (b)), with a CPW and a PGL port. If by combining the two S-parameter matrices of the half-PGL the results are the same as in the full CPW-PGL-CPW structure, then the PGL port would be considered valid. Results can be seen in Fig. 3.6.



(a)



(b)

**Figure 3.3:** (a) Impedance vs. ratio of outer/inner conductor radii for an ordinary coaxial cable and a dielectric-coated inner conductor coaxial cable, as depicted in Goubau's study [24]. (b) The impedance values vs. port size as obtained with the described PGL port in CST.

In Fig. 3.4, the S-parameters for 1 μm wide PGL deposited on a 30 μm thick BCB substrate were simulated in CST using several PGL port sizes. It shows that, for a port size value of 553 μm, the results converge, which means that the perfect conducting boundaries of the edges of the wave port are no longer influencing the Goubau mode at the PGL and thus a correct port size has been achieved.

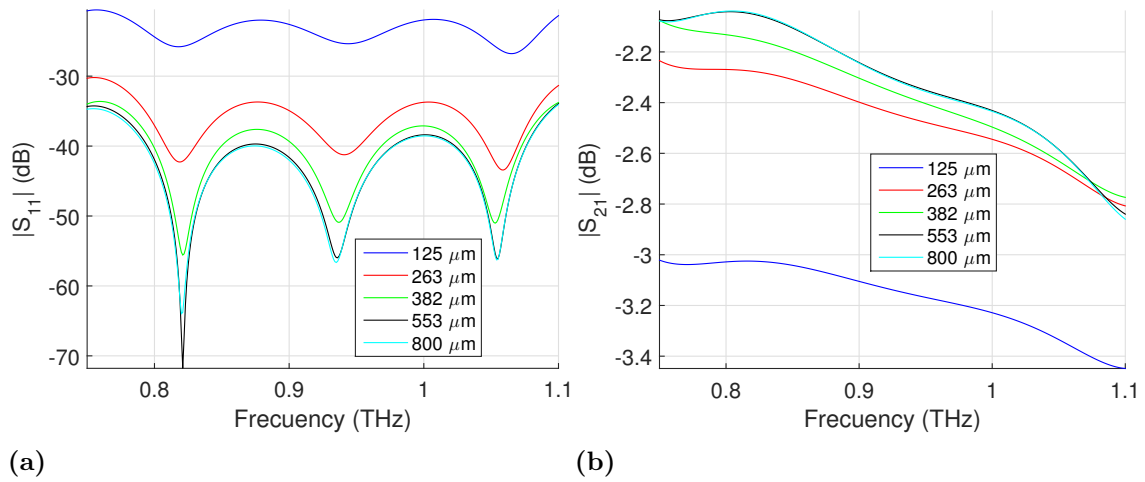


**Figure 3.4:** CST simulation results of (a)  $S_{11}$  and (b)  $S_{21}$  of a 1  $\mu\text{m}$  wide and 3 mm long PGL deposited on a 30  $\mu\text{m}$  thick BCB substrate for different port sizes. Results show to converge when the size of the port is increased.

The next step is to test if the results of the convergent PGL port are the same as the CPW wave-port. The structures shown in Fig. 3.5 (a) and (b) have been simulated in CST, where the half structure (Fig. 3.5 (b)) is cascaded with itself forming the complete structure (Fig. 3.5 (a)). The simulation results can be seen in Fig. 3.6, and show an approximate agreement between both approaches. These results validate the performance of the simulations done with the developed PGL port.

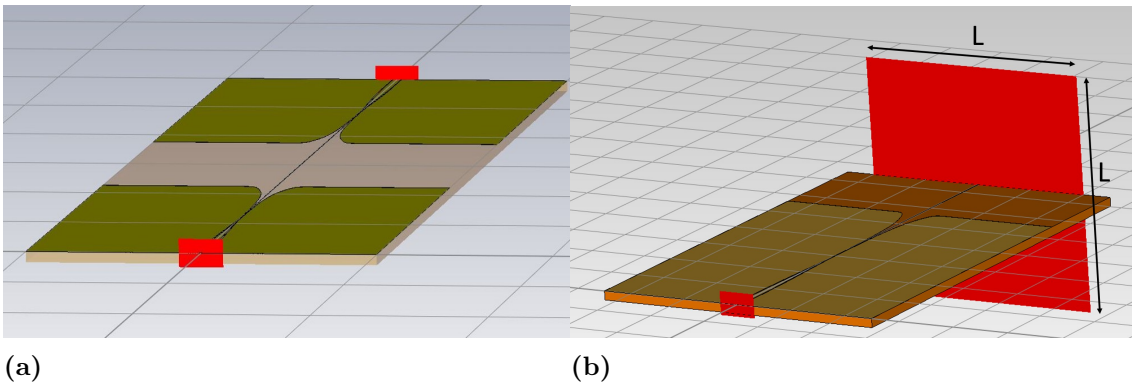


**Figure 3.5:** PGL port validity simulation, where a CPW-PGL-CPW structure (a) and half of the same structure using the PGL port (b) were simulated and compared in Fig. 3.6. The PGL port is square-shaped with side length of  $L$ .

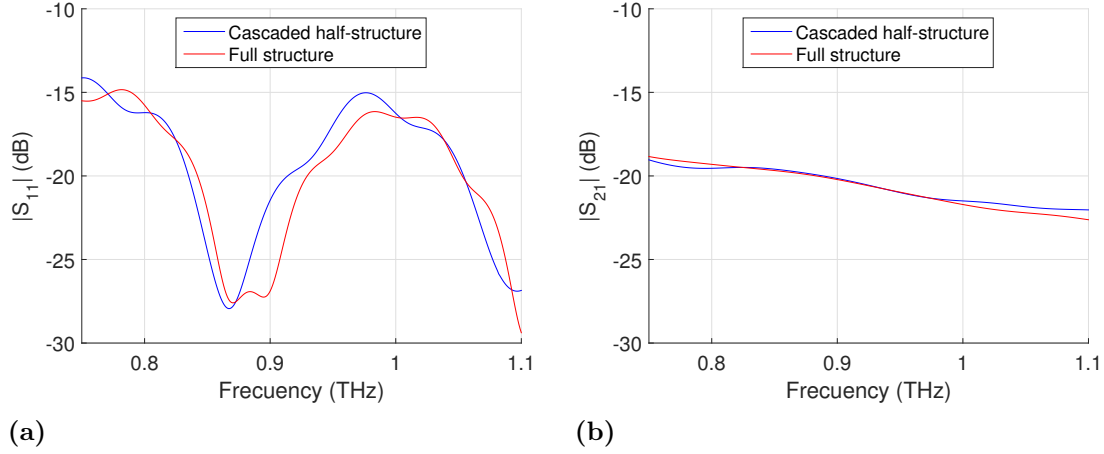


**Figure 3.6:** CST simulation results of (a)  $S_{11}$  and (b)  $S_{21}$  of the structures represented in Fig. 3.5.

Using the PGL wave-port described, a sufficiently large and convergent port was used to analyse the PGL port impedance value for a range of PGL widths. As it can be seen from the simulation results shown in Fig. 3.7, the value of the PGL impedance drops with increased PGL width.

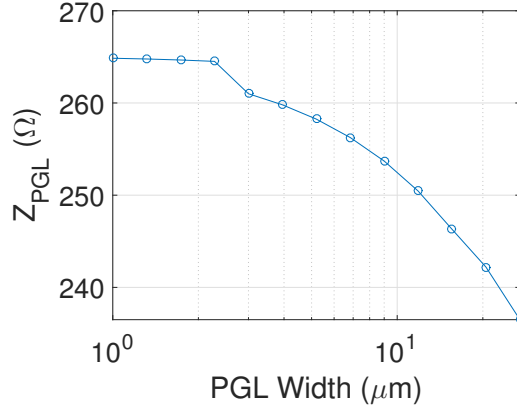


**Figure 3.7:** Simulated PGL characteristic impedance vs. PGL width, using the PGL port in CST.

### 3.2 Design of PGL

In this section, the key aspects of the PGL’s design have been explained for maximising transmission in the line and the amount of field on top of the substrate, with the purpose of increasing the sensitivity of the future sensor. The design parameters are substrate’s thickness and permittivity (section 3.2.1) and PGL’s width (section 3.2.2).

### 3.2.1 Choice of the substrate

The substrate plays a critical role in the electrical properties of the PGL. Its electrical properties (mainly the real and imaginary parts of the relative permittivity,  $\epsilon'_r(f)$  and  $\epsilon''_r(f)$ , respectively) affect the PGL's behaviour: adding dielectric losses, changing the electrical length, field distribution, etc. Additionally, the thickness of the substrate determines the cutoff frequency of the undesirable substrate modes. The following are desirable properties for the substrate:

- **Low dielectric constant:** reduces radiation losses [34], increases substrate modes cutoff frequency and increases field propagating on top of the substrate thus increasing sensitivity in the case of being used as a sensor.
- **Ultra-thin:** in the order of tens of microns, for the WR1.0 band, to avoid the coupling of substrate modes. The higher the frequency, the thinner the substrate needs to be [27, 29]. By limiting the number of parasitic modes that could be excited in the passive structure, it reduces losses and unwanted resonances.
- **Low attenuation:** to avoid power loss in the dielectric.
- **Low dispersion:** to prevent phase velocity differences within the frequency band.

Bearing these attributes in mind, the electrical properties of several materials available in the university's clean room were studied for making an adequate choice of the substrate. Benzocyclobutene (BCB) [34, 35] had low permittivity ( $\epsilon'_r \simeq 2.65$ ), low dispersion ( $\Delta\epsilon'_r \simeq 0.04$ ), low losses ( $\sim 2.3$  dB/mm at 1 THz), very thin substrate (tens of microns) and a simple fabrication process. These properties made it an ideal choice of substrate for THz frequencies. However, since it is a liquid which has to be deposited on a surface and cured, it needs a carrier wafer. To avoid losing its excellent properties, the BCB should be deposited on a wafer of a material which doesn't have an impact on the electrical behaviour of the structure. In [34] BCB was used as the substrate for a CPW at from 0.34 THz to 0.5 THz, using silicon as a carrier wafer, reporting losses of 3.5 dB mm<sup>-1</sup> at 0.5 THz. Since high-resistivity silicon showed in [36] to be a low loss material at THz frequencies, it was chosen as the carrier wafer material, to support the BCB layer. Thus, for this thesis, the substrate was chosen as a 30  $\mu$ m thick BCB layer deposited on a 300  $\mu$ m thick high-resistivity silicon wafer.

The cut-off frequency of the  $TM_0$  and  $TE_1$  dielectric slab modes for the BCB layer can be approximated using equations (2.6) and (2.7), and thus give an idea of when could the substrate mode be excited. Taking  $h = 30$   $\mu$ m and  $\epsilon'_r = 2.65$  yields in cut-off frequencies of 0 Hz for the  $TM_0$  mode and 1.95 THz for the  $TE_1$  mode. These results mean that the  $TM_0$  mode is unavoidable, but by using a thin substrate the  $TE_1$  will not be present in the frequency band used. To have a coupling from the CPW to a parasitic mode, in addition to being over the cut-off frequency, the phase constant in the parasitic mode needs to be higher than the one of the CPW mode.

### Influence of the carrier wafer

The impact of the high-resistivity silicon wafer was simulated in CST. Two simulations of a 3 mm long PGL were done, one in which the PGL substrate consists only of a 30  $\mu\text{m}$  thick BCB substrate and another one including a 300  $\mu\text{m}$  high-resistivity silicon substrate below the BCB. In both simulations, the substrate had a "*Open (add space)*", where CST adds a  $\lambda/4$  of air between the structures and an absorbing boundary.

Fig. 3.8 shows the simulation results. It can be concluded that the silicon will influence the performance of the PGL, where the  $S_{12}$  drops an average of 10 dB compared to the case without silicon. However, the silicon has shown to have little influence on the  $S_{11}$ .

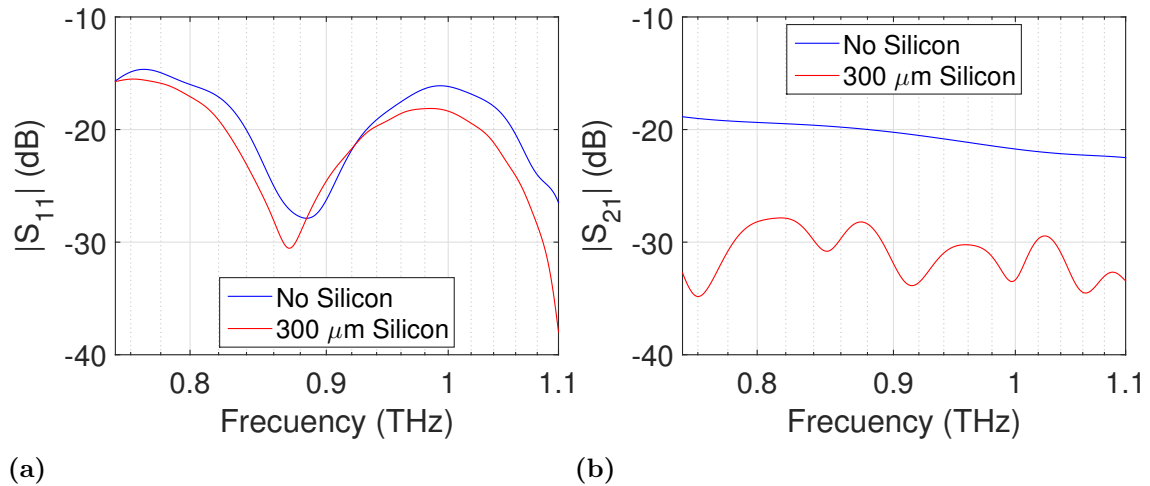


**Figure 3.8:** CST simulation results of (a)  $S_{11}$  and (b)  $S_{21}$  for a 3 mm long PGL on a 30  $\mu\text{m}$  thick BCB substrate with (in red) and without (in blue) a supporting 300  $\mu\text{m}$  high-resistivity silicon substrate below the BCB.

### 3.2.2 Width of the PGL

In most transmission lines there are several parameters which can be changed to modify its characteristics, e.g. line impedance. However, in a PGL the only parameter which can be modified in practice to vary the impedance along the line is the strip width. Therefore there is an interest in knowing its influence. According to [28]: "*under certain circumstances the thinner the G-Line strip, the higher the transmission level*", obtaining a measured 4 dB enhance of the  $S_{21}$  when using a 2  $\mu\text{m}$  instead of a 60  $\mu\text{m}$  wide PGL. In [26] explains the low attenuation of a single wire used for THz wave guiding by arguing that the conductor surface exposed to the field is much lower. A similar effect could happen in the PGL case, and therefore there is an interest in making the PGL line width narrow, in the order of 1 to tens of microns.

Several PGLs using different line widths (1  $\mu\text{m}$ , 3  $\mu\text{m}$  and 9  $\mu\text{m}$ ) have been simulated using CST. The substrate is made of 30  $\mu\text{m}$ /300  $\mu\text{m}$  thick BCB/Silicon layers,

and an absorbing boundary condition was set below the silicon substrate. The simulation results show, in Fig. 3.9, how there is a better transmission for the 3  $\mu\text{m}$  wide line, of about approximately 4–5 dB better than the 1 and 9  $\mu\text{m}$  wide lines. Since the transmission hasn't changed in a steady way against the PGL's width, it suggests that there are several factors which might impact the line transmission depending on the line width. Measurements will be performed to validate these results and to extract further conclusions.

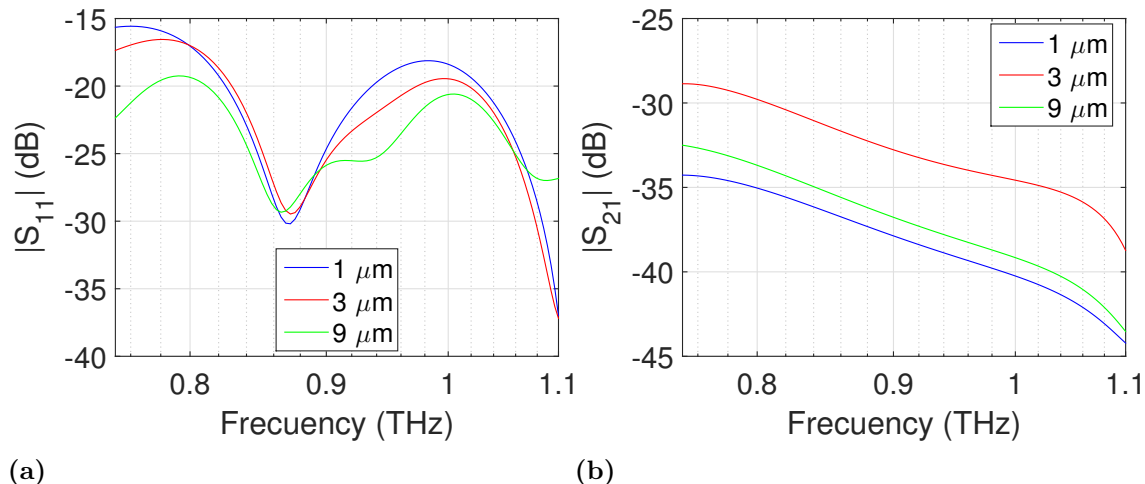


**Figure 3.9:** CST simulation results of (a)  $S_{11}$  and (b)  $S_{21}$  of 3 mm long a PGL of different widths: 1 (blue), 3 (red) and 9  $\mu\text{m}$  (green).

### 3.3 Design of CPW to PGL transition

The probes used to excite the planar structures have a Ground-Signal-Ground (GSG) contact geometry, which makes the CPW the natural transmission line to be used for contact with the probes. To excite the PGL, a CPW to PGL transition is necessary [19, 28, 37]. The design of this transition is crucial for an efficient Goubau mode excitation, where Akalin et al. reported that their CPW to PGL transition produced the most losses in their structures [19]. The transition can be seen as a device which gradually couples the CPW's even mode to a radial Goubau mode, while the CPW's grounds are lost progressively. The transition consists of three sections (see Fig. 3.10):

1. **CPW line:** it will be the contact region with the probe, and therefore its dimensions need to be fit for the probe pitch,  $p_p = 25 \mu\text{m}$ , and have a characteristic impedance of  $Z_0 = 50 \Omega$  to avoid reflections with the probe [15]. It also needs to excite the CPW even mode preventing other parasitic modes.
2. **Tapered CPW line:** gradually reduces the CPW line width to the desired PGL width, trying to minimise reflections.
3. **Launcher:** gradually separates the CPW grounds to excite the Goubau mode while minimising reflections.

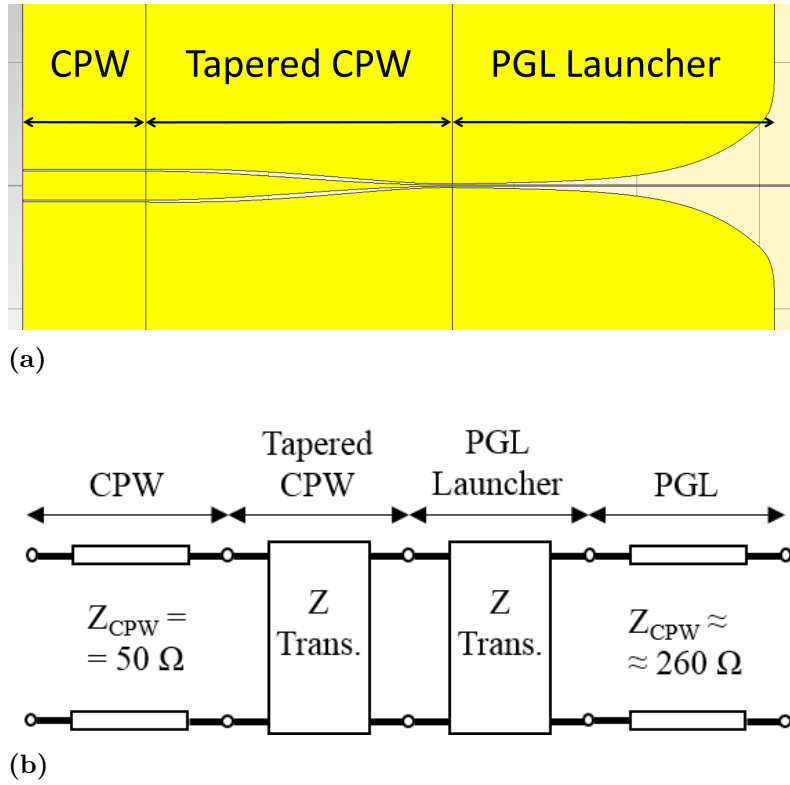


**Figure 3.10:** CPW to PGL transition split in its three sections. (a) Layout of transition. (b) Transmission line model of the CPW-PGL transition, using impedance transformers.

### 3.3.1 Design of probing CPW

For the CPW's design used to make contact with the RF-probes at least three things need to be considered:

1. **CPW gap:** the slot width ( $w_{CPW}$ ) needs to be smaller than  $10^\circ = \lambda/36$  at our highest frequency. For 1.1 THz and an approximate value of  $\epsilon_{eff} = 1.7$ , the slot width,  $w_{CPW}$ , needs to be smaller than  $5.8 \mu\text{m}$ .
2. **Fabrication limits:** the smallest features achievable are about  $5 \mu\text{m}$  for photolithography and  $30 \text{ nm}$  for electron beam lithography (beam size of  $5 \text{ nm}$ ).
3. **Size of probes:** the probe needs to be able to contact correctly the CPW, therefore the CPW line width ( $s_{CPW}$ ) needs to be larger than the probe contact pad ( $\sim 18 \mu\text{m}$ ), and the distance from the centre of the CPW line to the ground plane needs to be smaller than the probe pitch.

Since the CPW impedance is a function of both the strip and the slot width, there is one degree of freedom. Thus the condition  $s_{CPW} + w_{CPW} = p_p$  was imposed so that the probe's contact pads would be at the same distance to the slot in the CPW. Subsequently, the strip and slot widths were tuned using analytical expressions to obtain a  $Z_0 = 50 \Omega$  line, and giving final values of  $s_{CPW} = 23.5 \mu\text{m}$  and  $w_{CPW} = 1.5 \mu\text{m}$ , which satisfy the condition  $s_{CPW} + w_{CPW} = p_p$ .

### 3.3.2 Design of tapered CPW

The PGL line is physically an extension of the CPW's central strip. As explained before, the CPW strip width needs to be designed to allow the GSG probes to contact it, while in PGL, there is an interest in making the line width in the order of microns for minimising losses. Thus, the CPW's strip width,  $s_{CPW}$ , needs to be progressively changed to have the same width as the PGL's strip,  $s_{PGL}$ .

In this thesis, the change of strip width was made by using a cosine function (see Fig. 3.11) from  $s_{CPW}$  to  $s_{PGL}$  so that both in the beginning and end of the tapered section,  $ds/dx = 0$ , being  $x$  the PGL's longitudinal distance. The CPW's slot width was then calculated so it would have a smooth impedance transition from the  $Z_0 = 50 \Omega$  start CPW to the  $Z_{launcher} = \sqrt{Z_0 \cdot Z_{PGL}}$  CPW impedance just before the launcher<sup>1</sup>.

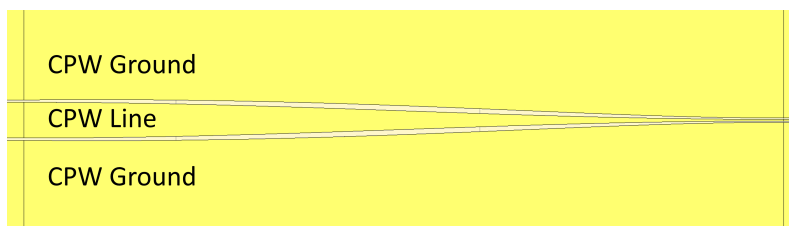


**Figure 3.11:** Designed CPW tapered line. The CPW strip width varies as a cosine function, while the slot width is adjusted to make a smooth impedance transition to minimize reflections.

To design a low-reflective tapered transmission line, a change of impedance between two arbitrary impedance values,  $Z_0$  and  $Z_{N+1}$  respectively, through  $N$  short-length transmission lines, is considered to model the tapered line (see Fig. 3.12). The impedances of each of the  $N$  transmission lines were designed to have equal partial reflection coefficients values for all line interfaces in the transition. Calculating the reflection coefficient for a high number of cascaded transmission lines requires many repeated calculations. However, since the impedance difference between contiguous lines is small (i.e.  $|Z_{n+1} - Z_n| \ll |Z_{n+1} + Z_n|$ ) for a high number of intermediate impedance values, *theory of small reflections* [21] was used for approximating the reflection coefficient, which simplified calculations without losing accuracy for all practical purposes.

<sup>1</sup>A middle impedance value between the initial  $Z_0$  and the final  $Z_{PGL} \sim 200 \Omega$ [19], to minimize reflections.

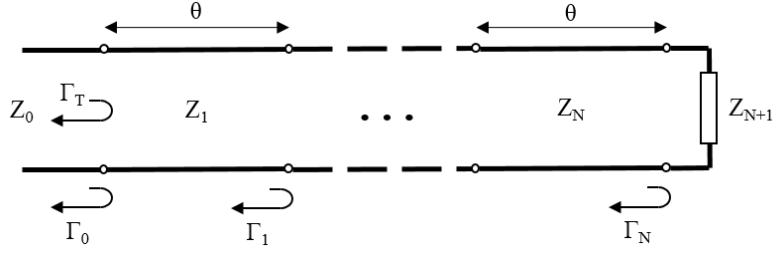


**Figure 3.12:** Impedance transformer between two arbitrary impedances,  $Z_0$  and  $Z_{N+1}$ . To model a tapered CPW impedance transformer a high value of  $N$  and small value of  $\theta$  are taken.

Let  $\Gamma_n$ , for  $0 \leq n \leq N$ , be the partial reflection coefficient between the lines  $n$  and  $n + 1$ . Since the design of  $Z_n$  was made imposing  $\Gamma_i = \Gamma_j \quad \forall i, j$  we can then refer to it simply as  $\Gamma$ . Then, using equation (2.4), the impedance values of the transmission lines are related as:

$$Z_n = \frac{1 - \Gamma}{1 + \Gamma} Z_{n+1} \quad (3.1)$$

and generalising

$$Z_n = \left( \frac{1 + \Gamma}{1 - \Gamma} \right)^n Z_0 \quad (3.2)$$

The value of  $\Gamma$  is still unknown, but it can be easily derived knowing that:

$$Z_{N+1} = \left( \frac{1 + \Gamma}{1 - \Gamma} \right)^{N+1} Z_0$$

$$\frac{1 + \Gamma}{1 - \Gamma} = \left( \frac{Z_{N+1}}{Z_0} \right)^{\frac{1}{N+1}} \quad (3.3)$$

which using (3.2) and (3.3) leads to the final expression of:

$$Z_n = \left( \frac{Z_{N+1}}{Z_0} \right)^{\frac{n}{N+1}} Z_0 \quad (3.4)$$

After obtaining the values of  $Z_n$  for  $1 \leq n \leq N$ , the CPW's slot width can be calculated for each of the  $N$  transmission lines in the tapered CPW to achieve the desired impedance, thus creating the low reflection tapered transition.

By using these values of  $Z_n$ , we obtain a total reflection,  $\Gamma_T$ , at the interface between  $Z_0$  and the  $N$ -line impedance transformer which, if  $|\Gamma| \gg |\Gamma|^2$ , can be approximated by small reflection theory as:

$$\Gamma_T \simeq \sum_{n=0}^N \Gamma_n e^{-j2\theta n} = \Gamma \sum_{n=0}^N e^{-j2\theta n} = \Gamma \frac{e^{j2\theta} - e^{-j2\theta N}}{e^{j2\theta} - 1} \quad (3.5)$$

where  $\Gamma$  can be obtained from rearranging (3.3):

$$\Gamma = \frac{\sqrt{Z_{N+1}} - \sqrt{Z_0}}{\sqrt{Z_{N+1}} + \sqrt{Z_0}} \quad (3.6)$$

Note that  $\Gamma_T$  will be equal to zero when:

$$2\pi k - 2N\theta = 2\theta; \quad \theta = \frac{\pi}{N+1}k \quad \forall k = 1, 2, \dots \quad (3.7)$$

which can be expressed in terms of the impedance transformer's total length,  $l_T$ :

$$l_T = N\theta \frac{\lambda}{2\pi} = k \frac{\lambda}{2} \frac{N}{N+1} = \{N \rightarrow \infty\} = k \frac{\lambda}{2} \quad \forall k = 1, 2, \dots \quad (3.8)$$

which means that if the  $N$ -line impedance transformer has a total length multiple of half a wavelength, there will be no reflection, at least for one frequency point. However, if the electrical length,  $\theta$ , of each of the  $N$  lines which form the impedance transformer is a multiple of  $\lambda/2$ , then a theoretical maximum reflection would be expected:

$$e^{j2\theta n} = 1 \quad \forall n \iff \theta = k\pi; \quad \text{or} \quad l_T = kN \frac{\lambda}{2} \quad (3.9)$$

which it will have a maximum reflection value,  $\Gamma_T = (N+1)\Gamma$ . However, for practical purposes, the electrical length of each section of the impedance transformer will be much smaller than  $\lambda/2$  and this maximum reflection value should not appear in any practical case. In Fig. 3 the total reflection was plotted against the total electrical length in wavelengths of the impedance transformer, showing how every  $\lambda/2$  there is a minimum in reflection, and that they decrease the longer the tapered becomes.

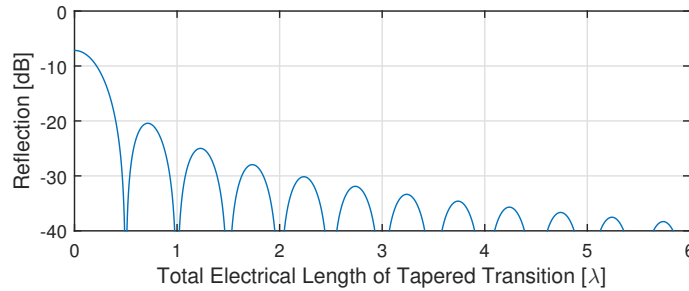


**Figure 3.13:** Reflection vs. total electrical length of a gradual impedance transformer between  $Z_0 = 50 \Omega$  and  $Z_{N+1} = 120 \Omega$ , modelled as a 1000-section transmission line. Below  $-40$  dB reflections can't usually be measured and thus are not plotted.

If there is a restriction on the maximum return losses,  $\Gamma_{max}$ , one can find the minimum length necessary to satisfy the return losses conditions in the following way:

1. Calculate the total reflection as a function of the tapered section's total electrical length,  $\Gamma_T(\theta_T)$ .
2. Calculate the regions where  $\Gamma_T(\theta_T) < \Gamma_{max}$ .

3. Calculate the relative bandwidth of the places where  $\Gamma_T(\theta_T) < \Gamma_{max}$  and compare to the bandwidth of the system to be designed. If  $\Gamma_T(\theta_T) < \Gamma_{max}$  between the values  $\theta_1 < \theta_T < \theta_2$ , and  $\theta_2/\theta_1 > f_{max}/f_{min}$ , being  $f_{max}$  and  $f_{min}$ , the maximum and minimum frequency in the band respectively, it will mean that the reflections will satisfy the condition for all the band for that region.

This way one can calculate the shortest tapered section which satisfies the return losses requirements and avoids adding unnecessary line losses. However, if the transmission level is to be maximised, an optimal value of the tapered CPW's length needs to be found for minimising the sum of the line losses and reflections, which limits transmission.

#### 3.3.3 Design of PGL launcher

To convert the CPW line to a PGL, the CPW's grounds have to be separated progressively to excite the Goubau mode. The launcher was designed by making a tapered slot width to separate the ground planes, trying to make the transition smooth to reduce return losses (see design in Fig. 3.14). The tapered launcher design was done in the following way:

1. A final separation between the CPW's ground planes,  $D$  in Fig. 3.14, was chosen based on the extension of the field of the Goubau mode. For an efficient mode conversion, the ground planes need to end sufficiently distant from the PGL to have no interaction with it.
2. The impedance of the CPW at the end of the launcher was calculated.
3. For transitioning from the initial to the end CPW in the launcher, an  $N$ -line impedance transformer was used to model the launcher. The impedances of each of the  $N$  lines were calculated using the method described in the previous section for the CPW tapered line. The total length of the launcher,  $L$  in Fig. 3.14, should be chosen as a multiple of  $\lambda/2$  for minimising reflections, as shown in Fig. .
4. The CPW's slot width was calculated using the obtained impedance value for each transmission line calculated in the previous step. The central strip has a constant width through the transition equal to the PGL line width,  $1\ \mu\text{m}$ .
5. Having all the slot widths dimensions over distance, the tapered ground planes can be drawn, which will be used for launching the Goubau mode. The last step would be to stretch the curve to fit the desired length of the launcher, which poses a trade-off between line losses and line reflections.

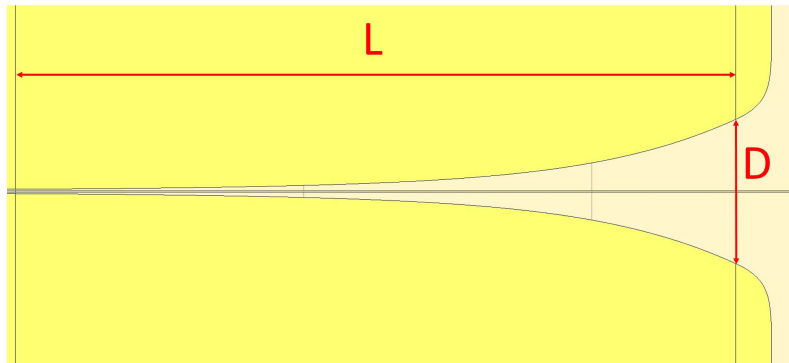


**Figure 3.14:** Tapered PGL launcher layout, where the central strip has a width of  $S_{PGL} = 1 \mu\text{m}$ .  $D$  is the final separation of the CPW grounds and  $L$  is the length of the launcher, respectively. An additional section was used to end the launcher with soft corners.

Also, at the end of the PGL launcher, the corners of both sides of the ground planes included a small section used to remove sharp edges on the launcher, to reduce radiation losses.

### 3.4 Fabrication process

In this section, the information about the fabrication process is presented. The fabrication was done in the clean room facilities at the Department of Microtechnology and Nanoscience of Chalmers University of Technology.

#### Wafer preparation

The fabrication starts by coating a 2-inch high-resistivity (2-5 k $\Omega$  cm) silicon wafer with a Cyclotene<sup>2</sup> layer, which will be our substrate. Before curing the Cyclotene, it was exposed to UV light. Since it is a negative photopolymer, this will protect it from the acetone during the lift-off. For curing the Cyclotene a dedicated furnace with a N<sub>2</sub> atmosphere was used. The fabrication steps were the following:

- Spin Cyclotene (XUS 35078 Type 03) at 1300 rpm for 60 s with an acceleration time of 5 s. This gives a thickness of about 30  $\mu\text{m}$  (Fig. 3.15(a) step 1).
- Bake on hot-plate at 100 °C for 90 s.
- Flood expose using UV light for 9 min.
- Cure on furnace at 250 °C for 60 min.

#### E-beam Lithography

The layout fabrication was done with e-beam lithography<sup>3</sup>, using a double layer of positive resist Copolymer/PMMA. Also, a layer of E-Spacer is used to evacuate the accumulated electrons in the substrate, to avoid surface charging. Since the layout has large exposed areas close to small unexposed areas, proximity compensation was

<sup>2</sup>Photopolymer derived from BCB.

<sup>3</sup>Raith EBPG 5200 was used, which has a beam size of 5 nm.

### 3. Method

used to prevent overexposure of the unexposed areas. The fabrication steps were the following (represented in Fig. 3.15):

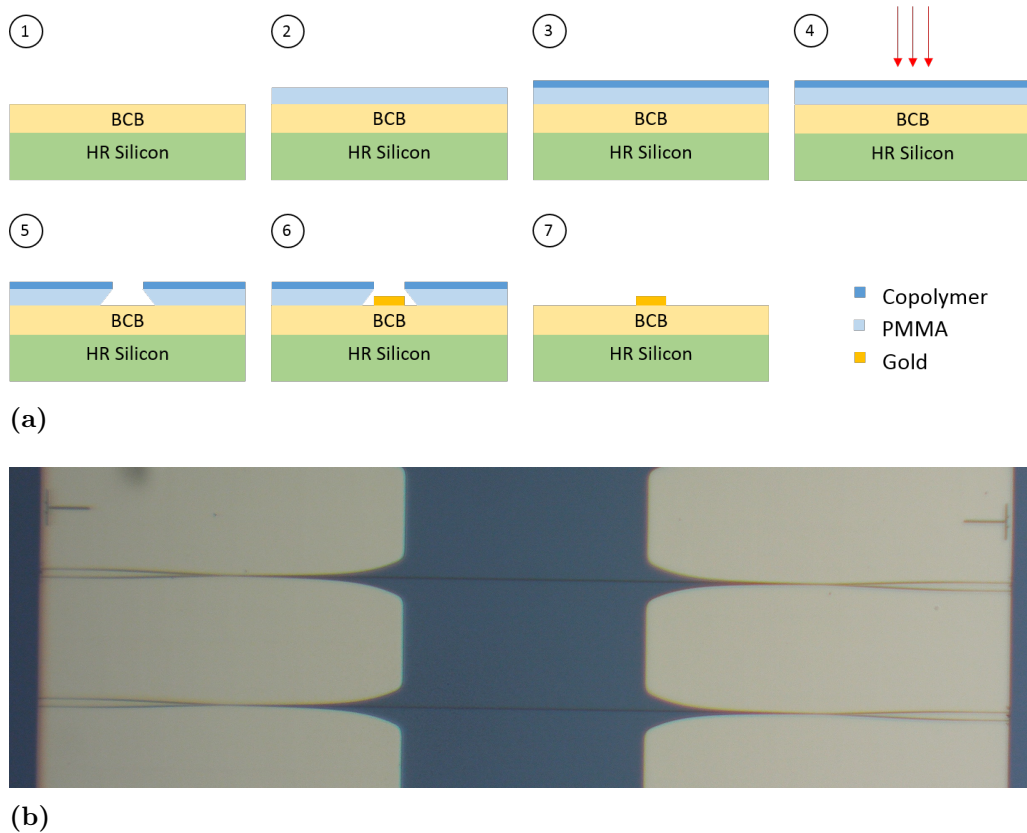


**Figure 3.15:** (a) Fabrication steps for e-beam lithography and (b) detail from the fabricated structure, showing 3 mm PGL structures.

- Spin NANO Copolymer 10% in Ethyl Lactate at 3000 rpm for 90 s with an acceleration time of 1 second. This gives a thickness of about 450 nm (Fig. 3.15(a) step 2).
- Bake on hotplate at 170 °C for 5 min.
- Spin NANO PMMA 2% in Anisole at 3000 rpm for 90 s with an acceleration time of 1 s. This gives a thickness of about 60 nm (Fig. 3.15(a) step 3).
- Bake on hotplate at 170 °C for 5 min.
- Spin E-Spacer 300Z at 1500 rpm for 60 s with an acceleration time of 1 s. Bake at 80 °C for 90 s on hotplate.
- E-beam exposure using 100 kV, 20 nA and with initial dose 450  $\mu\text{C}/\text{cm}^2$  (Fig. 3.15(a) step 4).
- Rinse E-Spacer 300Z with DI water.
- Develop in Isopropanol + DI Water (10:1) for 45 s (Fig. 3.15(a) step 5).
- Stop development using pure Isopropanol.
- Resist ash in oxygen plasma at 40 W for 10 s.
- Evaporate<sup>4</sup> 20 nm Ti/350 nm Au (Fig. 3.15(a) step 6).

<sup>4</sup>Using Lesker Spectros e-gun evaporator.

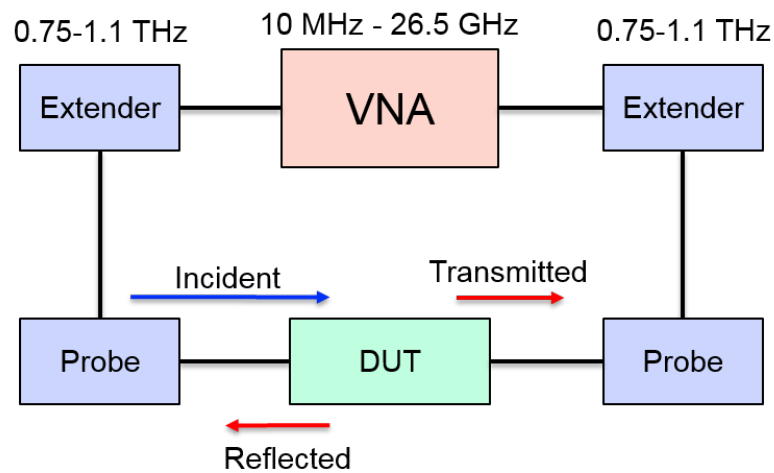
- Lift-off in Acetone (Fig. 3.15(a) step 7).

The dimensions of the structures were verified under the microscope, being the specified in the design. The fabrication yield resulted in about 80%.

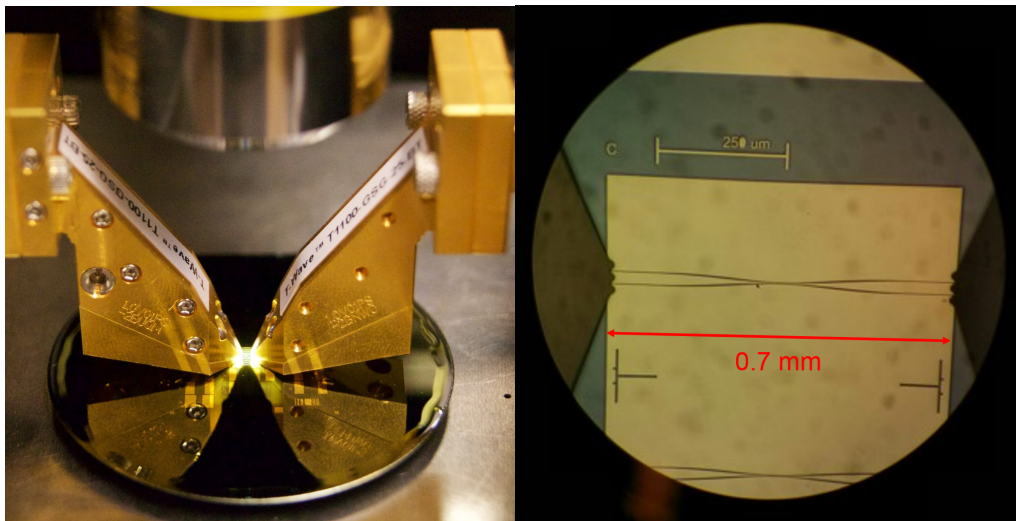
### 3.5 Measurement's set-up

For characterising the designed 2-port passive structures, on-wafer S-parameters measurements were performed. A sketch of the measurement set-up used can be seen in Fig. 3.16 (a), and includes:

- **Vector Network analyser (VNA):** an instrument which calculates S-parameters by measuring magnitude and phase of the incident, transmitted and reflected waves into a device under test (DUT) by sweeping the input signal over a frequency span. The signals are then converted to an intermediate frequency (IF) which are measured and displayed. The process of measuring is alternated between the channels of the VNA: first introducing the input signal into the DUT's port-1 and measuring S11 and S21, following by a switching the frequency sweep and measurement into port 2 and measuring S22 and S12. The VNA used for the measurements was a Keysight N5242A (10 MHz to 26.5 GHz) setting up an IF frequency of 10 Hz for achieving a low noise ground.
- **Frequency extenders:** when measuring S-parameters at THz frequencies, to generate high-frequency signals multipliers are used to convert the VNA's signal into a higher frequency signal, covering the band which needs to be measured. The frequency multiplication is achieved by using non-linear elements, which produce harmonics of an input signal, and later every signal is filtered except for the desired harmonic. Since most of the power is not in the desired harmonic, the process of frequency conversion comes with the price of a (typically) high conversion loss, which increases with the multiplication factor. The multiplication factors used in this case are 81 and 72 for RF and LO signals respectively and achieved frequencies from 0.75 THz to 1.1 THz. The frequency extenders used were VDI WR1.0SAX.
- **External RF and LO sources:** used instead of the internal VNA sources to achieve a higher dynamic range (about 5 dB gain) in the measurements thanks to their ultra low phase noise characteristics. When using multipliers to achieve higher frequencies, the phase noise deteriorates, and thus strict specifications on phase noise have to be imposed to the sources at this frequency band. The external sources used were Keysight E8257D (250 KHz to 20 GHz). The RF and LO output power were set to 7 dBm and  $-4$  dBm respectively.
- **Ground-Signal-Ground (GSG) Probes:** used as the interface between the frequency extenders and the DUT, the probes convert the rectangular waveguide from the extenders to a CPW line which terminates in the GSG tips which are used to couple the field into the structures to be measured. Cascade's T-Wave probes [15] were used for measuring between 0.75 THz and 1.1 THz (WR 1.0 band) and have a probe pitch of 25  $\mu\text{m}$ .



(a)



(b)

(c)

**Figure 3.16:** (a) Sketch of on-probe S-parameter measurements used. (b) Probes measuring the structures on the 2-inch BCB/Silicon wafer. (c) View of a tapered CPW being measured with the probes, as seen under the microscope.

The structures were measured on top of an absorbing material, which was placed on the probe station's metal chuck.

### 3.5.1 Calibration

The calibration is done to move the measuring planes to the point of interest, subtracting the effect of all components placed before the calibration plane. Several calibration methods exist, each of them using different elements to do the calibration. For THz frequencies, the commonly used calibration method is the Through-Reflect-Line (TRL) [38], since it does not need absorbing loads (Match) which are hard to fabricate at these frequencies. As its name suggests, the TRL calibration method needs:

- Through: a zero length transmission line. The calibration plane is located in the middle of the Through.
- Reflect: a highly reflective element i.e. an open-circuit or short-circuit.
- Line: a quarter-wave line at the central frequency. The difference in phase between the through and the line has to be between  $20^\circ < \phi < 160^\circ$  in all our band.

For measuring at these frequencies, there is a commercially available substrate. But since its substrate is made of a different material (quartz) it provides an artificial environment when calibrating using TRL. This is because the calibration plane is located in the middle of the Through line of the quartz substrate and thus a quartz Through line would be subtracted from the BCB structures measured, creating measurement artefacts. To avoid an artificial environment, a customised calibration substrate was designed and fabricated on the same BCB substrate as the structures being measured. Additionally, for achieving higher accuracy the Multi-Line TRL Method [39] was used, with the only difference with TRL that more transmission lines are included. This method lowers random errors which can happen in probing repeatability and improves precision and bandwidth over the single line TRL. The electrical length used for the two additional lines were  $3\lambda/4$  and  $11\lambda/4$  ( $190\ \mu\text{m}$  and  $697\ \mu\text{m}$  respectively).

Results showing a comparison of using the commercial substrate against the designed calibration substrate can be found in section 4.1.



# 4

## Results

This chapter will present the S-parameter measurements' results of the designed and fabricated structures in this thesis; it has been divided into three sections. First, an assessment of the repeatability of the measurements will be shown. Secondly, measurement results will be compared with two different simulation method results, to evaluate their accuracy for this case. And finally, presenting measurement results of the PGL to characterise its most relevant parameters. Such parameters include the PGL and CPW line's length, the length of the tapered CPW and PGL launcher and the PGL's width.

All structures, including the calibration ones, are contained in a single 2-inch wafer consisting of three layers: 350 nm gold, 30  $\mu\text{m}$  BCB and 300  $\mu\text{m}$  thick high-resistivity silicon wafer, as described in 3.4. The wafer was placed on top of an absorbing material to avoid reflection from the metal chuck in the measurements' set-up. All S-parameter measurements in this chapter have been done using RF-probes, as described in section 3.5.

### 4.1 Repeatability of the measurements

In this section, the reproducibility of the measurements is analysed. It is important to obtain the same results under similar conditions to trust the measurement results. For testing the repeatability, a 2.7 mm long PGL design has been measured using different calibrations, calibration substrates (commercial quartz and own design on BCB) and using several IF bandwidths. Table 4.1 shows the parameters used for each of the five S-parameter measurements shown in Fig. 4.1.

Parameters for measurements in Fig. 4.1			
Meas. #	Cal. Subs.	Cal. #	IF bandwidth
1	Quartz	1	100 Hz
2	Quartz	2	100 Hz
3	BCB	3	100 KHz
4	BCB	3	100 KHz
5	BCB	4	10 Hz

**Table 4.1:** Parameters used for the measurements. In order, the measurement number in Fig. 4.1, the calibration substrate used for the measurement, the calibration number and the IF bandwidth used.

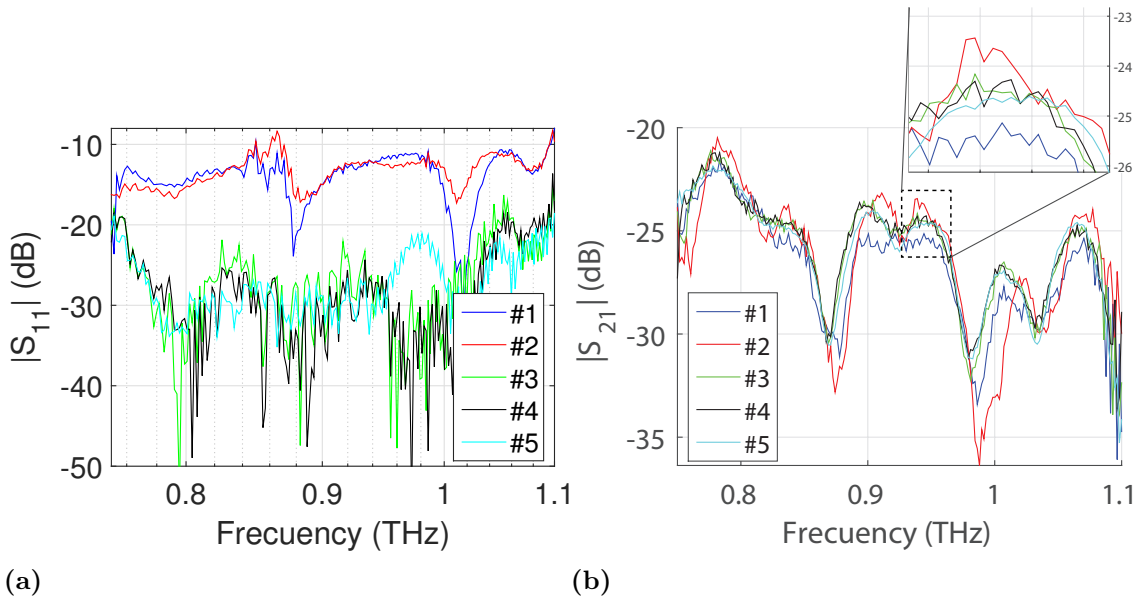


**Figure 4.1:** Five (a)  $S_{11}$  and (b)  $S_{21}$  measurements of the 2.7 mm long PGL structures using the measuring parameters in table 4.1. (Detail) Measurements from the BCB calibration substrate (# 3 to #5) are very repeatable, while the quartz ones (# 1 and #2) deviate more.

The measurements results of  $S_{11}$  show good repeatability within each calibration substrate. It was observed that the measurements done by calibrating using the commercial quartz calibration substrate (# 1 and #2) gave higher  $S_{11}$  values, which could be a product of having the calibration plane in the middle of the Through on the quartz calibration substrate. On the other hand, the measurements done by calibrating using the BCB calibration substrate (# 3 to #5) gave lower values of  $S_{11}$ , which corresponded with the expected values of an adequate coupling of the probe to the CPW followed by a low-reflective CPW-PGL transition. Since using the self-designed BCB calibration substrate did not introduce the artefacts added by the quartz substrate, all subsequent measurements were done using the BCB calibration substrate, in addition to an IF bandwidth of 10 Hz, since it increased the signal to noise ratio.

The measurements show good repeatability on  $S_{21}$  regarding their configuration, but it can be seen that the measurements done calibrating with the quartz calibration substrate (# 1 and #2) deviate more than the other measurements, done using the BCB calibration substrate.

## 4.2 Simulations vs. measurements

It is important to validate the simulations and compare the results of the different electromagnetic simulators considered in this thesis. For doing so, two structures (a 3 mm CPW and a 3 mm PGL) were simulated using CST and HFSS and also measured experimentally (results are shown in Fig. 4.2). Despite the absorbing material located below the silicon wafer during the measurements, measurement results show

periodic resonances which suggest the existence of reflections between the interfaces. The permittivity difference between the silicon and absorber could have produced reflections. The boundary conditions in the simulation which modelled better the measurement results was a perfect conducting boundary in the silicon's bottom side and not an absorbing boundary.

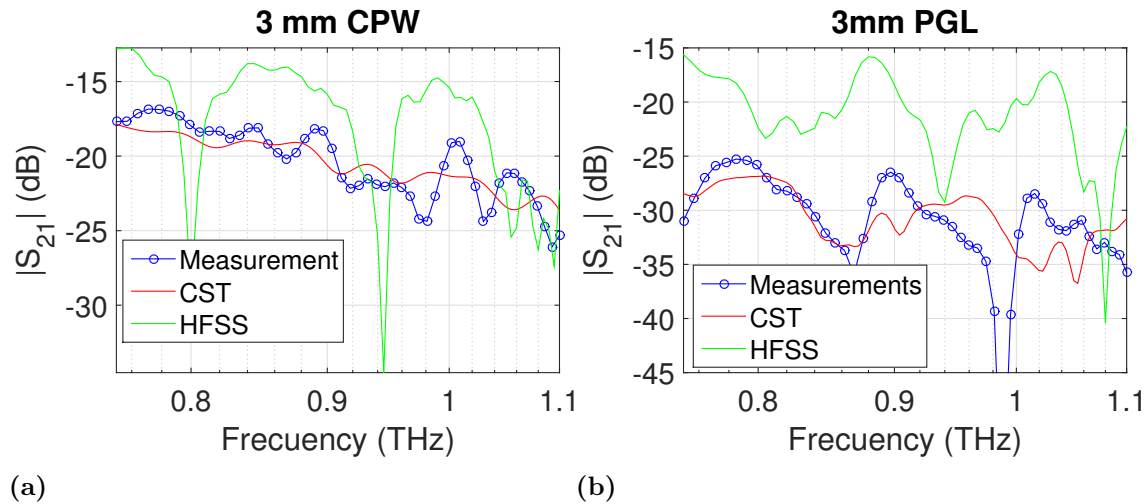


**Figure 4.2:**  $S_{21}$  results comparison of HFSS (green), CST (red) and VNA measurements (blue) of a 3 mm long CPW (a) and a 3 mm long PGL (b).

The results in Fig. 4.2 show that CST models the frequency response of the structures better than HFSS. To achieve higher agreement between simulations and measurements, the absorbing material placed under the wafer in the measurements could be modelled better, since an absorbing boundary condition did not show to represent its behaviour.

### 4.3 Characterisation of the PGL

In this section, the designed and fabricated PGL structures are characterised using RF-probe S-parameter measurements. First, the measurement results of a reference 3 mm long PGL are displayed. In the following sections, the measurement results of several structures are shown for the purpose of characterising key parameters in the PGL, including the lengths of PGL, CPW, tapered CPW and PGL launcher, and the width of the PGL.

#### 4.3.1 3mm long PGL

The physical dimensions of a 3 mm long PGL together with the S-parameter measurement results are presented in Fig. 4.3. The presented PGL will serve as a reference in this chapter when comparing with other structures.

## 4. Results

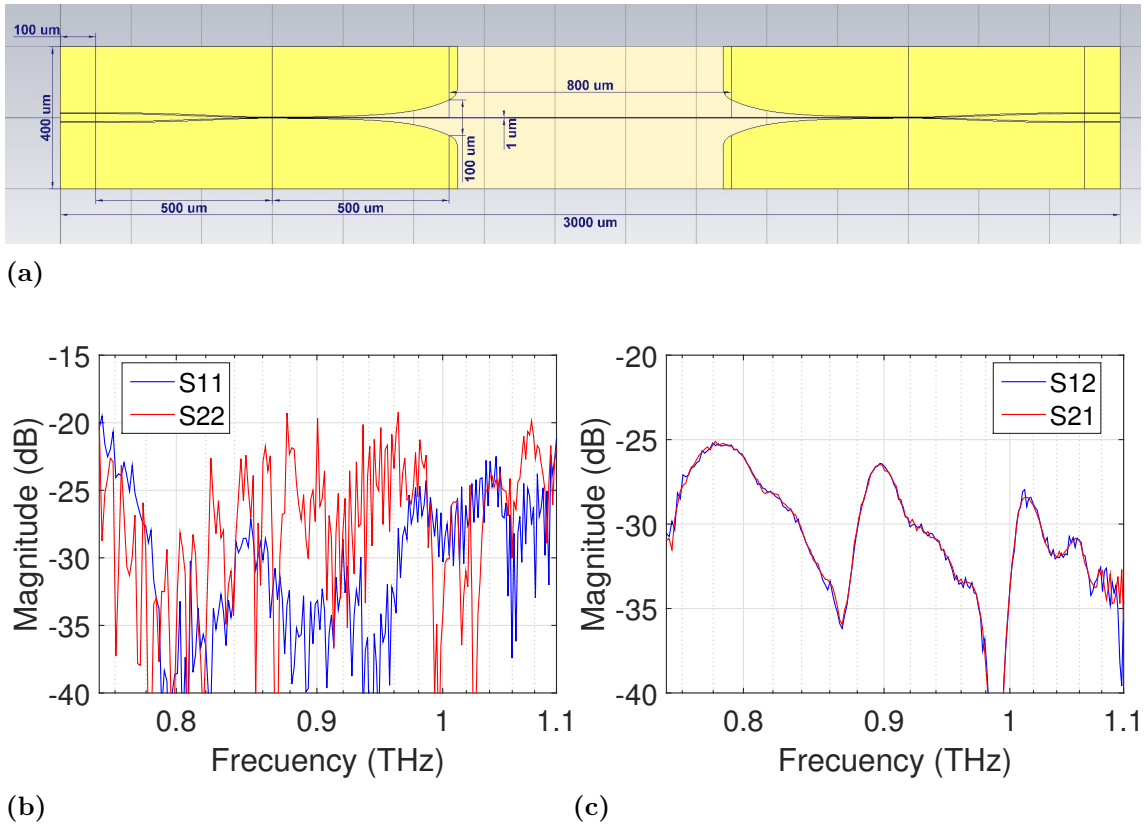


**Figure 4.3:** (a) Layout of the 3 mm long PGL. (b)  $S_{11}$  (blue) &  $S_{22}$  (red) and (c)  $S_{12}$  (blue) &  $S_{21}$  (red) measurement results.

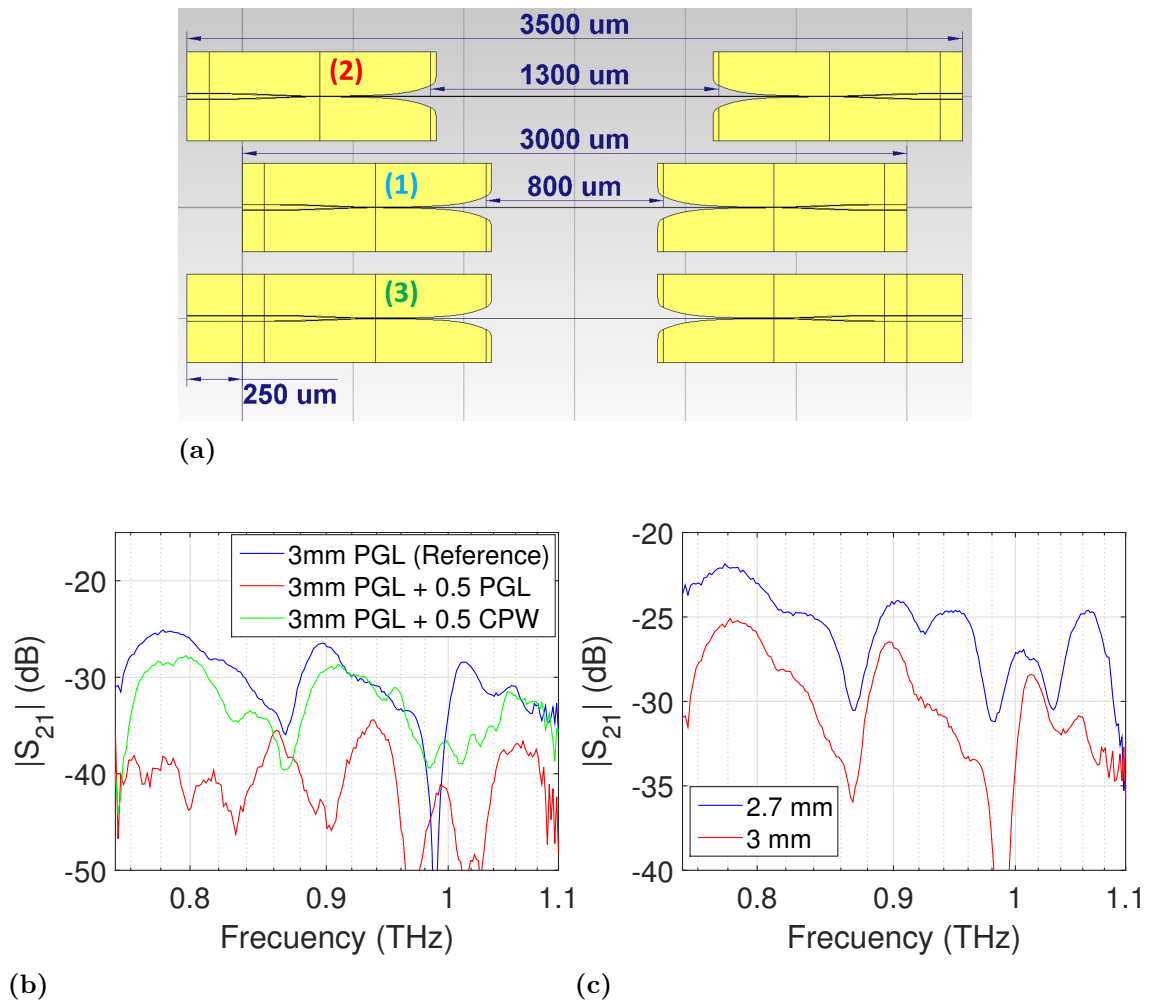
It can be seen that  $S_{11}$  and  $S_{22}$  stand below  $-20$  dB and show discrepancies between them, despite measuring a symmetrical passive structure. On the other hand, the transmission parameters are less noisy and fulfil reciprocity. If an average transmission value of  $-30$  dB is assumed, the losses per length are  $-10$  dB/mm, which shows good transmission for these frequencies.

### 4.3.2 Length of the CPW and PGL

Since the PGL needs a CPW transition to be excited using GSG probes, it is of interest to compare the losses of the CPW and PGL at these frequencies. For comparing the difference between two 500 μm long line sections of a CPW and a PGL, three cases were considered:

- A PGL of length 3 mm, (1) in Fig. 4.4 (a). It will serve as a reference.
- A PGL of length 3 mm, plus 500 μm extra PGL, (2) in Fig. 4.4 (a).
- A PGL of length 3 mm, plus 500 μm extra CPW, (3) in Fig. 4.4 (a).

In this way we can compare the losses from the CPW to the ones from the PGL, having both the same CPW-to-PGL transition.



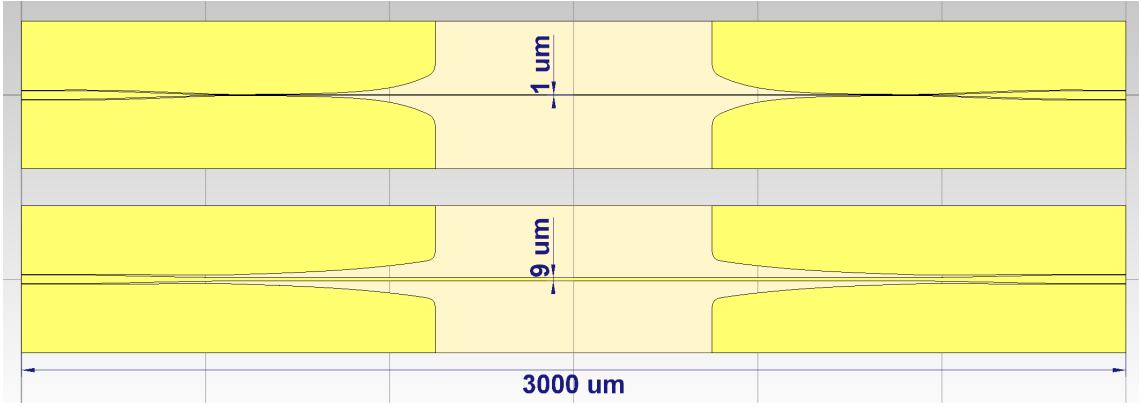
**Figure 4.4:** (a) Layout of the measured structures in Fig. 4.4 (b). (b)  $S_{21}$  measurements of reference (blue), plus 500  $\mu\text{m}$  extra PGL (red) and plus 500  $\mu\text{m}$  extra CPW (green). (c)  $S_{21}$  measurements of the reference 3 mm long PGL (red) and a 2.7 mm long PGL (blue), having both the same CPW-PGL transition.

Fig. 4.4 (b) shows a drop of about 2 to 3 dB in  $S_{21}$  when adding 0.5 mm of CPW to structure (1), and about 7 to 10 dB when adding 0.5 mm of PGL. Since adding 0.5 mm of PGL to structure (1) drops considerably  $S_{21}$ , to better characterise the losses per unit length of the PGL, the measurement results of a 2.7 mm PGL is also compared to the reference 3 mm PGL, in Fig. 4.4 (c). Fig. 4.4 (c) shows an approximate 4 dB average difference between the  $S_{21}$  of both lines, giving an approximate loss value for the PGL of 13.3 dB/mm. From Fig. 4.4 (b) the CPW losses can be estimated to approximately 5 dB/mm. These results suggest limiting the use of the PGL for sensing and using the CPW for a more efficient power transmission.

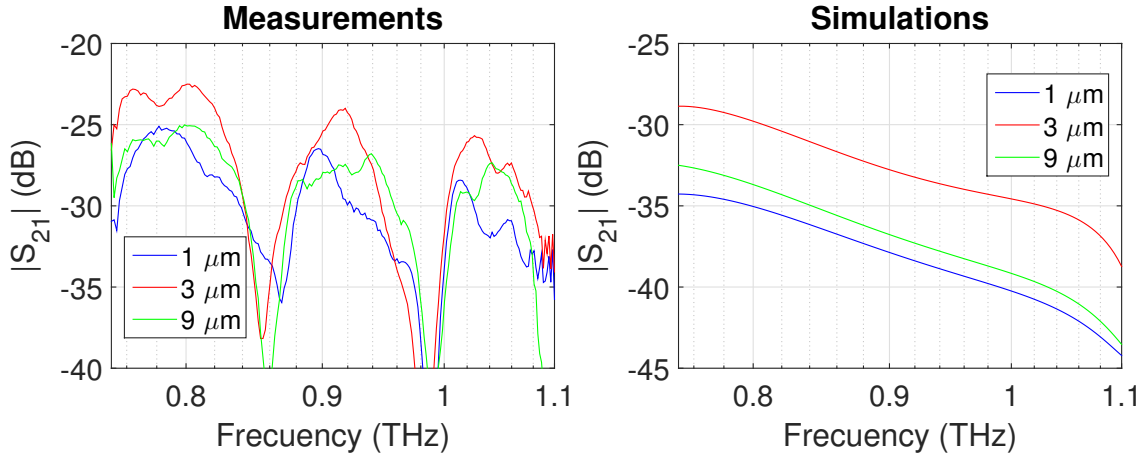
### 4.3.3 Width of the PGL

The width is a design parameter which can be easily varied in the PGL, and thus studying its impact over frequency is of interest. Several 3 mm long PGLs were

designed using three different PGL widths ( $1\ \mu\text{m}$ ,  $3\ \mu\text{m}$  and  $9\ \mu\text{m}$ ). The measurement results of these PGLs can be seen in Fig. 4.5.



(a)



(b)

(c)

**Figure 4.5:** (a) Layout of the  $1\ \mu\text{m}$  and  $9\ \mu\text{m}$  wide PGL structures. (b)  $S_{21}$  measurements of  $1\ \mu\text{m}$  (blue),  $3\ \mu\text{m}$  (red) and  $9\ \mu\text{m}$  (green) wide PGLs. (c) Simulated  $S_{21}$  results of  $1\ \mu\text{m}$  (blue),  $3\ \mu\text{m}$  (red) and  $9\ \mu\text{m}$  (green) wide PGLs using an absorbing condition on the bottom side of the silicon substrate.

The S-parameter measurements in Fig. 4.5 show similar behaviour for all three compared PGL widths. Resonances are maintained and the transmission level is approximately 2 dB higher in the  $3\ \mu\text{m}$  width line than in the other cases and a similar result can be seen from simulation results. A steady increase/decrease in transmission level was expected with line width variation; however, a higher transmission level was observed for the intermediate width value ( $3\ \mu\text{m}$ ), which suggests that several factors influence the transmission level.

#### 4.3.4 Length of the tapered CPW

To have higher power reaching the PGL, the tapered CPW was designed to maximise its transmission. There are two factors which lower the value of  $S_{21}$ : the first is

return losses, which are inversely proportional to the section's length, as an abrupt line width change causes reflections; and the second is line losses, which are directly proportional to the section's length. In this section, the  $S_{21}$  measurements of two tapered CPWs with lengths  $250\ \mu\text{m}$  and  $500\ \mu\text{m}$  are compared to estimate which losses are more relevant. The  $250\ \mu\text{m}$  tapered CPW will have lower line losses while the  $500\ \mu\text{m}$  will have lower reflection losses.  $250\ \mu\text{m}$  and  $500\ \mu\text{m}$  correspond to electrical lengths of  $\lambda$  and  $2\lambda$ , respectively<sup>1</sup>, which have minimum reflection values as shown in Fig. 3.

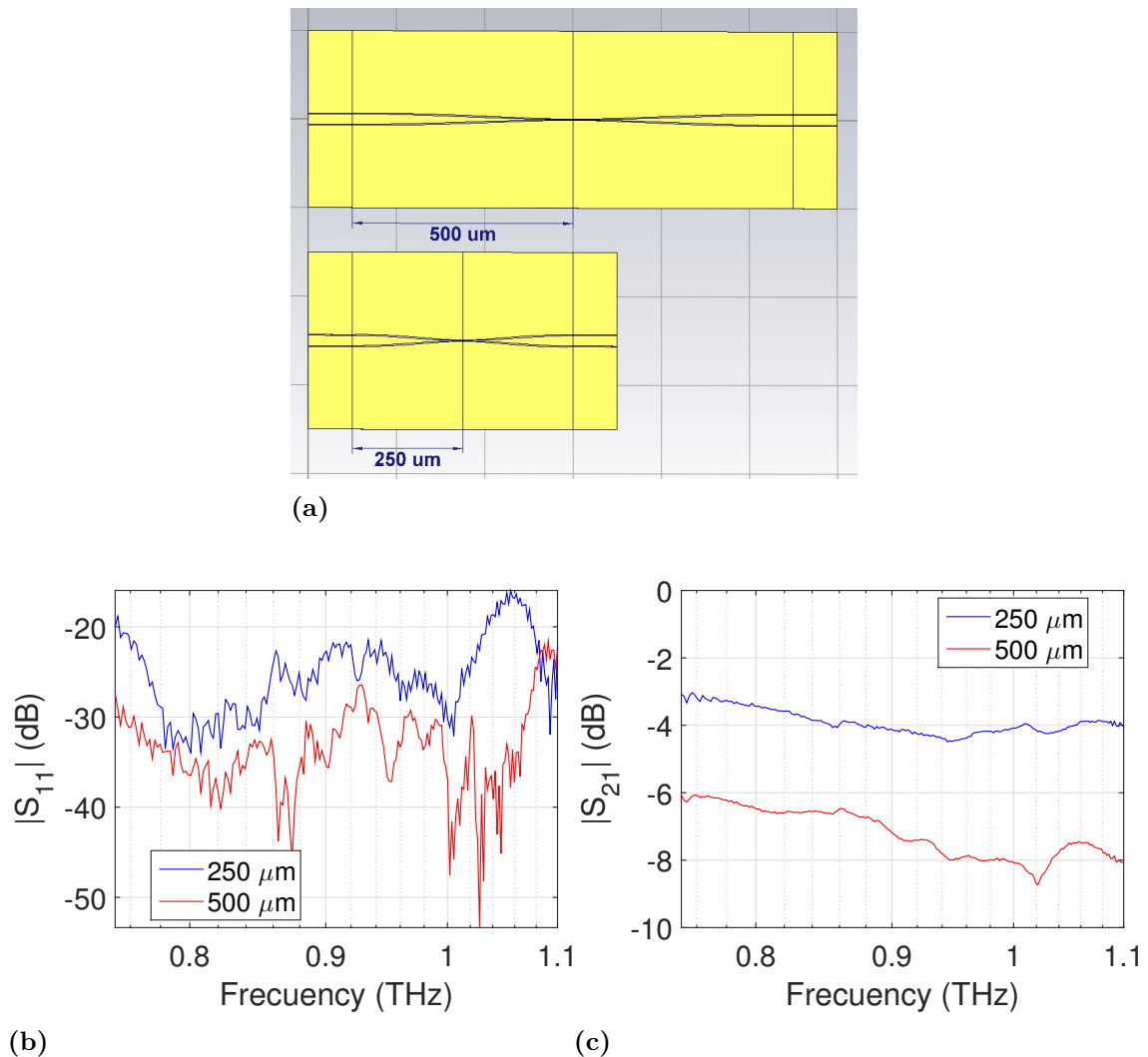


**Figure 4.6:** (a) Layout of the measured structures. (b)  $S_{11}$  and (c)  $S_{21}$  measurements comparison of  $250\ \mu\text{m}$  (blue) and  $500\ \mu\text{m}$  (red) long tapered CPWs.

Results in Fig. 4.6 show a higher transmission level for the shorter  $250\ \mu\text{m}$  tapered CPW than for the  $500\ \mu\text{m}$  long one, while reflection levels are slightly higher for the  $250\ \mu\text{m}$  tapered CPW. These results show that line losses are greater than the reflection losses for the compared lengths, and thus the CPW transition should be made smaller to maximise  $S_{21}$ .

<sup>1</sup>Considering a frequency of  $0.91\ \text{THz}$  and a effective permittivity of  $\epsilon_{eff} = 1.7$

### 4.3.5 Length of the PGL launcher

With the same purpose of maximising transmission in the CPW-PGL transition, the influence of the length of the PGL launcher was also studied for two cases: 250  $\mu\text{m}$  and 500  $\mu\text{m}$  long PGL launchers, (see design layout in Fig. 4.7). By comparing the two structures, one can obtain information of the necessary length for the PGL launcher to be efficient and maximise the transmission to the PGL.

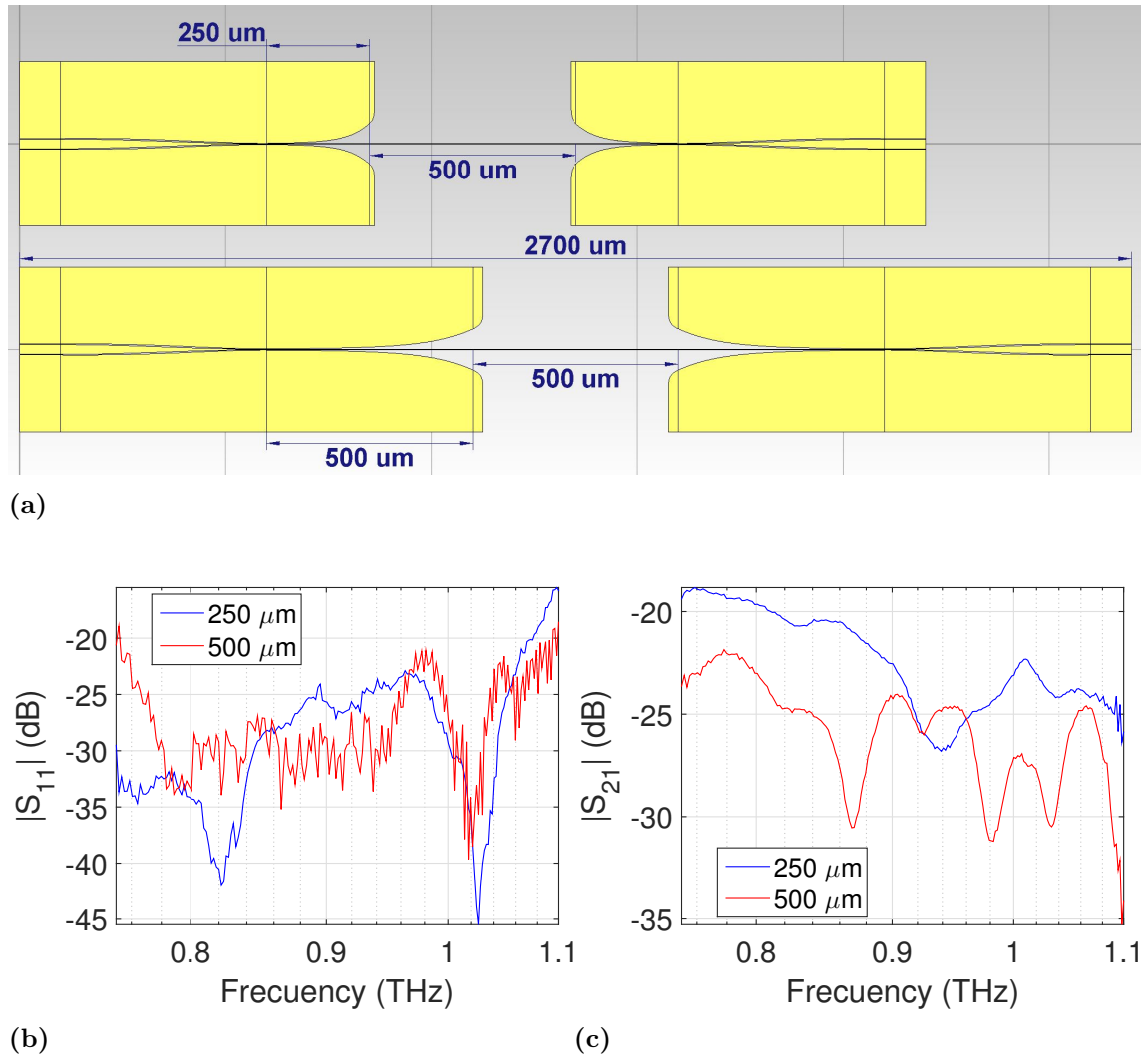


**Figure 4.7:** (a) Layout of the measured structures. (b)  $S_{11}$  and (c)  $S_{21}$  measurements comparison of 250  $\mu\text{m}$  (blue) and 500  $\mu\text{m}$  (red) long PGL launchers.

Fig. 4.7 shows a higher  $S_{21}$  level for the 250  $\mu\text{m}$  long launcher than for the 500  $\mu\text{m}$  long one, while reflections are practically at the same level. Therefore, the line losses are higher than the return losses for the chosen PGL launcher lengths; hence the shorter launcher will increase transmission.

# 5

## Conclusion

In this thesis, a PGL and its transition from CPW have been designed, fabricated and measured between 0.75 THz and 1.1 THz as part of an effort for developing THz biosensors based on planar structures and excited using RF-probes and a VNA.

When working at THz frequencies, the thickness and permittivity of the substrate are critical to avoid the coupling of substrate modes, minimise losses and maximise sensitivity. In this thesis, a 30  $\mu\text{m}$  BCB substrate ( $\epsilon_r = 2.65$  and  $\alpha = 2.3$  dB/mm) on top of a 300  $\mu\text{m}$  Silicon wafer ( $\epsilon_r = 11.7$  and  $\alpha = 0.035$  dB/mm) that provides mechanical support was the selected substrate. For exciting the PGL with RF probes, a transition from a 50  $\Omega$  CPW to the PGL that minimises reflections was designed using transmission line theory.

To create an accurate simulation environment, frequency-domain FEM and time-domain FIT simulations were compared. Particular attention was paid to the port excitation, critical when performing electromagnetic simulations at THz frequencies. For the structures done in this thesis and the frequency band under consideration, time-domain FIT using wave ports was selected as the simulation method as it gave better agreement with the experimental results with affordable simulation time.

The structures were fabricated in the cleanroom of the Microtechnology and Nanoscience Department at Chalmers University using electron-beam lithography and characterised by on-wafer S-parameter measurements between 0.75 THz and 1.1 THz. TRL calibration structures were designed and fabricated on the same wafer as the PGLs.

S-parameter measurements showed good repeatability and low  $S_{21}$  and  $S_{12}$  noise level, however, a higher noise level was obtained for  $S_{11}$  and  $S_{22}$ . The measurement results of a 3 mm PGL showed an approximate average transmission of  $-10$  dB/mm between 0.75 THz and 1.1 THz showing some resonances which are believed to come from the substrate modes in the Si carrier wafer. The measured PGL losses had an average of 13 dB/mm while the ones measured for a CPW line in the same wafer and frequency range had an average of 5 dB/mm. In both cases, substrate modes and conductor losses are believed to be important contributors to total losses. The influence of the Si carrier wafer was studied with electromagnetic simulations, showing losses estimated in 3.3 dB/mm. Regarding the PGL's width, simulations and measurements agree that the 3  $\mu\text{m}$  wide PGL line has better transmission than a 1  $\mu\text{m}$  and a 9  $\mu\text{m}$  wide lines, which suggests that several factors are influencing the efficiency of the PGL against its width. The influence of the different parts of the PCW to PGL transition, taper and launcher were studied. Measurements showed that a 250  $\mu\text{m}$  long tapered CPW and PGL launcher have a higher transmission than a 500  $\mu\text{m}$  version. These results mean that line losses have a greater impact on

the transmission of the PGL than the reflections introduced by the CPW to PGL transition.

For future work, to achieve higher transmission levels, substrate modes in the carrier wafer need to be eliminated, possibly by using alternative ultra-thin substrates which don't need a carrier wafer. Besides, since losses in the CPW have shown to be smaller than in the PGL, the use of PGL needs to be limited to the sensing area and use the CPW when possible. More transmission could also be achieved by shortening the CPW-PGL transition and study the length which maximises the power delivered to the PGL. After optimising the power delivered to the PGL, resonators will be designed for increasing the sensitivity of the biosensor. These resonators together with the integration of a microfluidic device would allow analysing biological samples in their native environment, having a high degree of control of the sample volume and minimising losses derived from the contact with water. The proposed THz near-field system is expected to achieve greater sensitivity and higher dynamic range than present methods, increasing the possibilities of bio-analysis at THz frequencies.

# Bibliography

- [1] A. Davies, E. H. Linfield, and M. B. Johnston, “The development of terahertz sources and their applications,” *Physics in Medicine and Biology*, vol. 47, no. 21, p. 3679, 2002.
- [2] J. Ward, E. Schlecht, G. Chattopadhyay, A. Maestrini, J. Gill, F. Maiwald, H. Javadi, and I. Mehdi, “Capability of THz sources based on Schottky diode frequency multiplier chains,” *Microwave Symposium Digest, 2004 IEEE MTT-S International*, vol. 3, pp. 1587–1590, 2004.
- [3] S. Matsuura, G. A. Blake, R. A. Wyss, J. C. Pearson, C. Kadow, A. W. Jackson, and A. C. Gossard, “A traveling-wave THz photomixer based on angle-tuned phase matching,” *Applied Physics Letters*, vol. 74, no. 19, pp. 2872–2874, 1999.
- [4] P. H. Siegel, “Terahertz technology,” *IEEE Transactions on Microwave Theory and Techniques*, vol. 50, no. 3, pp. 910–928, Mar 2002.
- [5] D. T. Leisawitz, W. C. Danchi, M. J. DiPirro, L. D. Feinberg, D. Y. Gezari, M. Hagopian, W. D. Langer, J. C. Mather, S. H. Moseley Jr, M. Shao *et al.*, “Scientific motivation and technology requirements for the SPIRIT and SPECS far-infrared/submillimeter space interferometers,” *Astronomical Telescopes and Instrumentation*, pp. 36–46, 2000.
- [6] T. Kleine-Ostmann and T. Nagatsuma, “A review on terahertz communications research,” *Journal of Infrared, Millimeter, and Terahertz Waves*, vol. 32, no. 2, pp. 143–171, 2011.
- [7] J. F. Federici, B. Schulkin, F. Huang, D. Gary, R. Barat, F. Oliveira, and D. Zimdars, “THz imaging and sensing for security applications—explosives, weapons and drugs,” *Semiconductor Science and Technology*, vol. 20, no. 7, p. S266, 2005.
- [8] P. H. Siegel, “Terahertz technology in biology and medicine,” *IEEE Transactions on Microwave Theory and Techniques*, vol. 52, no. 10, pp. 2438–2447, Oct 2004.
- [9] A. Markelz, S. Whitmire, J. Hillebrecht, and R. Birge, “THz time domain spectroscopy of biomolecular conformational modes,” *Physics in Medicine Biology*, vol. 47, no. 21, p. 3797, 2002.
- [10] N. Laman, S. S. Harsha, D. Grischkowsky, and J. S. Melinger, “High-resolution waveguide THz spectroscopy of biological molecules,” *Biophysical Journal*, vol. 94, no. 3, pp. 1010 – 1020, 2008.
- [11] X. Yang, X. Zhao, K. Yang, Y. Liu, Y. Liu, W. Fu, and Y. Luo, “Biomedical applications of terahertz spectroscopy and imaging,” *Trends in Biotechnology*, vol. 34, no. 10, pp. 810 – 824, 2016.

- [12] S. P. Micken, A. Menikh, H. Liu, C. A. Mannella, R. MacColl, D. Abbott, J. Munch, and X. Zhang, "Label-free bioaffinity detection using terahertz technology," *Physics in Medicine and Biology*, vol. 47, no. 21, p. 3789, 2002.
- [13] M. Brucherseifer, M. Nagel, P. Haring Bolivar, H. Kurz, A. Bosserhoff, and R. Büttner, "Label-free probing of the binding state of DNA by time-domain terahertz sensing," *Applied Physics Letters*, vol. 77, no. 24, pp. 4049–4051, 2000.
- [14] M. Nagel, P. H. Bolivar, M. Brucherseifer, H. Kurz, A. Bosserhoff, and R. Büttner, "Integrated planar terahertz resonators for femtomolar sensitivity label-free detection of DNA hybridization," *Applied optics*, vol. 41, no. 10, pp. 2074–2078, 2002.
- [15] M. F. Bauwens, N. Alijabbari, A. W. Lichtenberger, N. S. Barker, and R. M. Weikle, "A 1.1 THz micromachined on-wafer probe," *2014 IEEE MTT-S International Microwave Symposium (IMS2014)*, pp. 1–4, June 2014.
- [16] K. Grenier, D. Dubuc, P.-E. Poleni, M. Kumemura, H. Toshiyoshi, T. Fujii, and H. Fujita, "Integrated broadband microwave and microfluidic sensor dedicated to bioengineering," *IEEE Transactions on Microwave Theory and Techniques*, vol. 57, no. 12, pp. 3246–3253, 2009.
- [17] H. Rodilla, A. Kim, G. Jeffries, J. Vukusic, A. Jesorka, and J. Stake, "Millimeter-wave sensor based on a  $\lambda/2$ -line resonator for identification and dielectric characterization of non-ionic surfactants," *Scientific Reports*, vol. 6, p. 19523, 2016.
- [18] S. Liu, I. Ocket, M. Cauwe, D. Schreurs, and B. Nauwelaers, "Sensitivity analysis of broadband on-wafer dielectric spectroscopy of yeast cell suspensions up to 110 GHz," *IEEE Microwave and Wireless Components Letters*, vol. 25, no. 3, pp. 199–201, 2015.
- [19] T. Akalin, A. Treizebré, and B. Bocquet, "Single-wire transmission lines at terahertz frequencies," *IEEE Transactions on Microwave Theory and Techniques*, vol. 54, no. 6, pp. 2762–2767, 2006.
- [20] D. M. Pozar, *Microwave engineering*. John Wiley & Sons, 2012.
- [21] R. E. Collin, *Foundations for microwave engineering*. John Wiley & Sons, 2007.
- [22] C. P. Wen, "Coplanar waveguide: A surface strip transmission line suitable for nonreciprocal gyromagnetic device applications," *IEEE Transactions on Microwave Theory and Techniques*, vol. 17, no. 12, pp. 1087–1090, 1969.
- [23] A. Sommerfeld, "Ueber die fortpflanzung elektrodynamischer wellen längs eines drahtes," *Annalen der Physik*, vol. 303, no. 2, pp. 233–290, 1899.
- [24] G. Goubau, "Single-conductor surface-wave transmission lines," *Proceedings of the IRE*, vol. 39, no. 6, pp. 619–624, 1951.
- [25] Y. Xu and R. Bosisio, "Study of Goubau lines for submillimetre wave and terahertz frequency applications," *IEEE Proceedings-Microwaves, Antennas and Propagation*, vol. 151, no. 5, pp. 460–464, 2004.
- [26] K. Wang and D. M. Mittleman, "Metal wires for terahertz wave guiding," *Nature*, vol. 432, no. 7015, pp. 376–379, 2004.
- [27] Y. Xu and R. G. Bosisio, "A study of planar Goubau lines (PGLs) for millimeter-and submillimeter-wave integrated circuits (ICs)," *Microwave and optical technology letters*, vol. 43, no. 4, pp. 290–293, 2004.

- 
- [28] A. Treizebré, T. Akalin, and B. Bocquet, “Planar excitation of Goubau transmission lines for THz bioMEMS,” *IEEE Microwave and Wireless Components Letters*, vol. 15, no. 12, pp. 886–888, 2005.
- [29] M. Spirito, G. Gentile, and A. Akhnoukh, “Multimode analysis of transmission lines and substrates for (sub) mm-wave calibration,” *Microwave Measurement Conference, 2013 82nd ARFTG*, pp. 1–6, 2013.
- [30] J.-M. Jin, *The finite element method in electromagnetics*. John Wiley & Sons, 2015.
- [31] Ansoft HFSS v17.2, *Ansoft Corporation, Pittsburgh, PA*, 2016.
- [32] T. Weiland, “A discretization model for the solution of Maxwell’s equations for six-component fields,” *Archiv Elektronik und Uebertragungstechnik*, vol. 31, pp. 116–120, 1977.
- [33] CST Microwave Studio 2017, *CST Computer Simulation Technology AG.*, 2017.
- [34] L. Cao, A.-S. Grimault-Jacquín, N. Zerounian, and F. Aniel, “Design and VNA-measurement of coplanar waveguide (CPW) on benzocyclobutene (BCB) at THz frequencies,” *Infrared Physics & Technology*, vol. 63, pp. 157–164, 2014.
- [35] E. Perret, N. Zerounian, S. David, and F. Aniel, “Complex permittivity characterization of benzocyclobutene for terahertz applications,” *Microelectronic Engineering*, vol. 85, no. 11, pp. 2276–2281, 2008.
- [36] D. Grischkowsky, S. Keiding, M. van Exter, and C. Fattinger, “Far-infrared time-domain spectroscopy with terahertz beams of dielectrics and semiconductors,” *J. Opt. Soc. Am. B*, vol. 7, no. 10, pp. 2006–2015, Oct 1990.
- [37] A. Treizebré, B. Bocquet, Y. Xu, and R. G. Bosisio, “New THz excitation of planar Goubau line,” *Microwave and Optical Technology Letters*, vol. 50, no. 11, pp. 2998–3001, 2008.
- [38] G. F. Engen and C. A. Hoer, “Thru-reflect-line: An improved technique for calibrating the dual six-port automatic network analyzer,” *IEEE Transactions on Microwave Theory and Techniques*, vol. 27, no. 12, pp. 987–993, 1979.
- [39] R. B. Marks, “A multiline method of network analyzer calibration,” *IEEE Transactions on Microwave Theory and Techniques*, vol. 39, no. 7, pp. 1205–1215, 1991.

